Seismic diffraction imaging to characterise mass-transport complexes: examples from the Gulf of Cadiz, south west Iberian Margin

This manuscript is pre-print submitted to EarthArXiv. The manuscript has been formally accepted for publication in Journal of Geophysical Research: Solid Earth. The final copy-edited and typeset version will be available via the Peer-reviewed Publication DOI link on the right-hand side of this webpage.

Please feel free to contact any of the authors, we welcome feedback:

Jonathan Ford[1,2] (jford@inogs.it)
Roger Urgeles[3] (urgeles@icm.csic.es)
Angelo Camerlenghi[1] (acamerlenghi@inogs.it)
Eulàlia Gràcia[3] (egracia@icm.csic.es)

[1]National Institute of Oceanography and Applied Geophysics (OGS)
[2]University of Trieste
[3]Institut de Ciències del Mar (CSIC)

Seismic diffraction imaging to characterise mass-transport complexes: examples from the Gulf of Cadiz, south west Iberian Margin

Jonathan Ford[1,2], Roger Urgeles[3], Angelo Camerlenghi[1], Eulàlia Gràcia[3]

[1]National Institute of Oceanography and Applied Geophysics - OGS
[2]Dipartimento di Matematica e Geoscienze, Università di Trieste
[3]Institut de Ciències del Mar, CSIC

Key Points:

- Seismic diffractions encode information about the small-scale internal structure of mass-transport complexes (MTCs).
- Diffraction images offer a low-cost route to improve the lateral resolution and effective vertical resolution of seismic images of MTCs.
- 2-D seismic profiles record out-of-plane diffractions generated by MTCs, which may be used to put minimum constraints on their 3-D geometry

Corresponding author: Jonathan Ford, jford@inogs.it

Abstract

Mass-transport complexes (MTCs) are often characterised by small-scale, discontinuous internal structure, such as slide blocks, rough interfaces, faults and truncated strata. Seismic images may not properly resolve such structure because seismic reflections are fundamentally limited in lateral resolution by the source bandwidth. The relatively weak seismic diffractions, instead, encode information on sub-wavelength scale structure with superior illumination. In this paper, we compare diffraction imaging to conventional, full-wavefield seismic imaging to characterise MTCs. We apply a seismic diffraction imaging workflow based on plane-wave destruction filters to two 2-D marine multi-channel seismic profiles from the Gulf of Cadiz. We observe that MTCs generate a large amount of diffracted energy relative to the unfailed confining sediments. The diffraction images show that some of this energy is localised along existing discontinuities imaged by the full-wavefield images. We demonstrate that, in combination with full-wavefield images, diffraction images can be utilised to better discriminate the lateral extent of MTCs, particularly for thin bodies. We suggest that diffraction images may be a more physically correct alternative to commonly used seismic discontinuity attributes derived from full-wavefield images. Finally, we outline an approach to utilise the out-of-plane diffractions generated by the 3-D structure of MTCs, normally considered a nuisance in 2-D seismic processing. We use a controlled synthetic test and a real data example to show that under certain conditions these out-of-plane diffractions might be used to constrain the minimum width of MTCs from single 2-D seismic profiles.

Plain Language Summary

Underwater landslides are a significant geohazard that can generate large magnitude tsunami and threaten seafloor infrastructure such as pipelines and telecommunication cables. The deposits from these events (so-called mass-transport complexes, or MTCs) can preserve internal structure that can reveal the dynamics of failure, important to understand the geohazard potential from future events. One common tool for investigating these deposits is seismic imaging, which uses recordings of seismic waves reflected and scattered from the subsurface to image the geology. The resolution of the reflected waves, however, is often too poor to properly characterise the complex, strongly deformed internal structure of MTCs. In this study, we instead use the seismic waves scattered at lateral, basal and internal discontinuities formed by landslide processes to produce diffraction images of MTCs. We show that these images have improved resolution and illumination of the small-scale structure. We suggest that diffraction imaging could be a useful tool for geohazard investigations of complex geology.

1 Introduction

Mass-transport complexes (MTCs) are the deposits of subaqueous mass-movements such as debris flows, slides and slumps (Prior et al., 1984; Mulder & Cochonat, 1996; Piper et al., 1997; Sawyer et al., 2009). Such events pose a significant geohazard to coastal populations from landslide-induced tsunami (Tappin et al., 2001; Satake, 2012) and to seafloor infrastructure such as telecommunications cables and pipelines (Piper et al., 1999; Carter et al., 2014). MTCs have important implications for hydrocarbon exploration as they form a significant proportion of deep-water sediment fill (Weimer & Shipp, 2004) and they can have both reservoir and seal potential (Alves et al., 2014; Cardona et al., 2016). They also represent a drilling hazard as they are often over-consolidated (densified) compared to unfailed sediments (Shipp et al., 2004).

MTCs can preserve complex, laterally discontinuous internal structure such as slide blocks, rough interfaces, faults and truncated strata (Lucente & Pini, 2003; Bull et al., 2009). These so-called *kinematic indicators* can record the dynamics of failure, transport and emplacement, important for constraining the flow type and the geohazard potential of future mass-movements. When the scale of this structure is close to the limit of seismic resolution, seismic images of MTCs can be difficult to interpret, often showing an apparently “chaotic” or “disordered” seismic character (Posamentier & Martinsen, 2011). This can be a problem when discriminating between different types of mass-movements, for example debris flow deposits (lacking internal bedding, chaotic seismic character) and slumps (internal bedding preserved but may still show a chaotic seismic character without sufficient seismic resolution). This can also make it difficult to characterise the amount and style of deformation within a deposit.

Efforts to improve the characterisation of internal structure from seismic images have largely relied on improvements in acquisition technology in recent decades. Industry-scale 3-D seismic surveys can provide the spatial resolution and coverage to observe large-scale internal structure within MTCs, particularly from plan-view time and depth slices (e.g., Frey Martinez et al., 2005; Bull et al., 2009; Gafeira et al., 2010; Lackey et al., 2018;

Steventon et al., 2019). In academic settings maximum offsets are typically limited relative to the target depth, meaning reflectors are often poorly illuminated, intrinsically limiting the lateral resolution. Improvements in imaging of academic data have typically come from novel acquisition geometries and seismic sources, such as ultra-high resolution deep-tow seismic (Badhani et al., 2020) and short-offset 3-D “P-cable”-type geometries (Berndt et al., 2012; Karstens et al., 2019). Such approaches can provide dramatic increases in seismic resolution within MTCs at the cost of significantly increased acquisition effort.

An alternative strategy to improve the interpretable resolution of existing seismic data is to apply quantitative interpretation techniques such as seismic attributes (Chopra & Marfurt, 2007). Seismic attributes can highlight discontinuities and identify areas of disrupted seismic reflectors by deriving statistical properties within data windows of seismic images. Such approaches have been applied to discriminate MTCs from background sedimentation (when they have chaotic internal seismic character) as well as to characterise the flow direction and assess the degree of internal disaggregation (e.g., Alves et al., 2014; Bhatnagar et al., 2019). Seismic attributes, however, are typically derived from full-wavefield seismic images, which suffer from the lateral resolution limits outlined above, and data windowing can reduce their effective resolution with respect to the original image.

Conventional seismic processing emphasises preserving and imaging the reflected seismic wavefield—the relatively weak diffracted wavefield is often ignored, aliased or accidentally attenuated (Klem-Musatov et al., 2016; Schwarz, 2019b). Seismic reflections cannot properly resolve geological structures smaller than the Rayleigh limit (i.e., half a seismic wavelength; on the order of metres to decametres for typical marine airgun data) (Born & Wolf, 1959; Chen & Schuster, 1999). Such structures, instead, scatter the seismic waves and generate diffractions, meaning that the diffracted wavefield can encode sub-wavelength information about small-scale subsurface discontinuities. Diffraction imaging works by separating the reflected and diffracted wavefields and migrating only the diffracted component, producing an image of these small-scale heterogeneities (Klem-Musatov et al., 2016; Schwarz, 2019b). Contrary to reflections, the radation pattern of diffractions is independent of the dip (Fig. 1), meaning that they can be fully illuminated even by short- or zero-offset receiver arrays (Preine et al., 2020). This radial spreading, combined with the general smaller scale of diffractors compared to reflectors means that, for a given seismic source, the recorded diffracted wavefield tends to be significantly weaker and have higher frequency content than the reflected wavefield. Consequently, the relatively high-amplitude, long-wavelength reflections can easily mask the diffractions in conventional, full-wavefield seismic images. Diffraction images therefore offer potentially improved lateral resolution and better illumination of small-scale, discontinuous geological structure. Several approaches for diffraction separation have been developed. Some exploit the difference in moveout of reflections and diffractions in common-shot or common-midpoint domains (Khaidukov et al., 2004), or the difference in dip and lateral continuity between reflections and diffractions in common-offset domain (Taner et al., 2006; Fomel et al., 2007; Decker et al., 2017). Others rely on wavefront attributes and the assumed coherence of seismic reflections to model and subtract the reflected wavefield (Dell & Gajewski, 2011; Schwarz & Gajewski, 2017). Another approach is to perform the separation during migration, exploiting the fact that in migrated dip-angle domain diffractions appear flat, whereas reflections appear as hyperbolae (Moser & Howard, 2008).

MTCs very often contain a large amount of potential diffractors: interfaces with width below the Rayleigh criterion (sub-wavelength scale heterogeneities) or near-infinite local curvature (edges, discontinuities and truncations) (Fig. 1a). Examples of such internal structure could include the hinges of slump folds (Alsop & Marco, 2013); offset across normal and reverse faults within extensional and compressional shear zones (Posamentier & Martinsen, 2011); wavelength-scale transported clasts (Talling et al., 2010); truncated reflectors at the boundaries of slide blocks (Sobiesiak et al., 2016); rough basal topography and ramp-and-flat structures (Lucente & Pini, 2003); headwall scarps (Bull et al., 2009) and steep, erosive lateral margins (Frey Martinez et al., 2005) (Fig. 1b). This points to the potential of seismic diffractions to encode unique information on the small-scale internal structure and the discontinuous external boundaries of MTCs. Indeed, the presence of diffraction tails (sometimes referred to as *hyperbolae*, although diffractions are only strictly hyperbolic when the overburden velocity structure is laterally homogenous) in unmigrated seismic and sub-bottom profiler data is often used as an indicator of mass-movements (Urgeles et al., 1999; Diviacco et al., 2006). Even MTCs that do preserve coherent, well-imaged internal strata or internal geometry may benefit from the superior illumination of diffractions, especially at the discontinuous basal surface, lateral margins and internal dislocation planes between slide blocks. Structural reconstruction to quantify strain distribution within MTCs relies on the proper imaging of such supra-seismic scale interfaces (Steventon et al., 2019; Bull & Cartwright, 2020).

Seismic diffraction imaging has been used to characterise a range of complex geological targets including faults, channels, pinchouts, rugose interfaces, karstic carbonate reservoirs and fracture zones (Fomel et al., 2007; Reshef & Landa, 2009; Decker et al., 2015; Schwarz & Krawczyk, 2020). In this paper we explore the potential of diffraction imaging to characterise the complex internal structure and external morphology of MTCs. This approach has the potential to increase the value of existing seismic data during processing at relatively low additional computational cost (comparable to a conventional migration). We apply diffraction imaging to two 2-D, multi-channel seismic profiles containing prominent MTCs from the Gulf of Cadiz (south west Iberian Margin). We first demonstrate the ability of diffraction images to resolve small-scale internal structure compared to conventional, full-wavefield seismic images. We then compare diffraction images to traditional seismic discontinuity attributes for identification and interpretation of relatively small, thin MTCs. Finally, we outline a speculative approach to utilise the illumination of out-of-plane diffractions (normally considered a nuisance) and the inherently 3-D structure of MTCs. We suggest that in certain conditions this out-of-plane diffracted energy might be used to constrain the minimum cross-line width of MTCs from single 2-D seismic profiles.

2 Geological Setting

The Gulf of Cadiz is located offshore the south west margin of the Iberian Peninsula and north west Morocco (Fig. 2). The region is characterised by active tectonics related to convergence between the African and Eurasian plates. The tectonic structure and seafloor morphology of the gulf is the result of an accretionary wedge formed from the Late Cretaceous to the Late Miocene (Zitellini et al., 2009). The accretionary wedge is covered by Late Miocene to Plio-Quaternary sediments, pierced by mud volcanoes and pockmarks (indicating active fluid flow) and salt diapirs (Gràcia, Dañobeitia, Vergés, Bartolomé, & Córdoba, 2003; Gràcia, Dañobeitia, Vergés, & Team, 2003; Zitellini et al., 2009; Medialdea et al., 2009). The Gulf of Cadiz and the south west Iberian Margin host large magnitude ($M_w > 8$) earthquakes (Gràcia et al., 2010; Matias et al., 2013) and submarine landslides (Urgeles & Camerlenghi, 2013). Both processes pose significant tsunami hazard to nearby coastal populations (Baptista & Miranda, 2009; Lo Iacono et al., 2012;

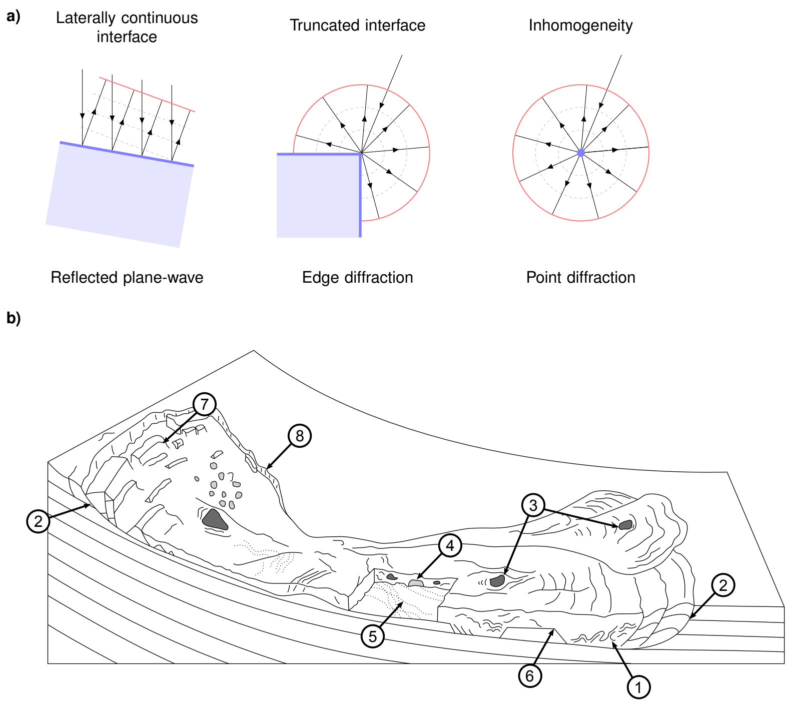

Figure 1. a) The 2-D radiation pattern of reflections from a laterally continuous interface compared to diffractions from truncations (infinite curvature *edge diffractors*) or sub-wavelength scale heterogeneities (*point diffractors*). b) Schematic diagram of an MTC labelled with discontinuous structure likely to generate seismic diffractions: 1) intense folding; 2) extensional and compressional shear zones; 3) transported clasts; 4) boundaries of slide blocks; 5) rough basal topography; 6) ramp-and-flat structures; 7) headwall scarps and 8) lateral margins (modified from Bull et al., 2009).

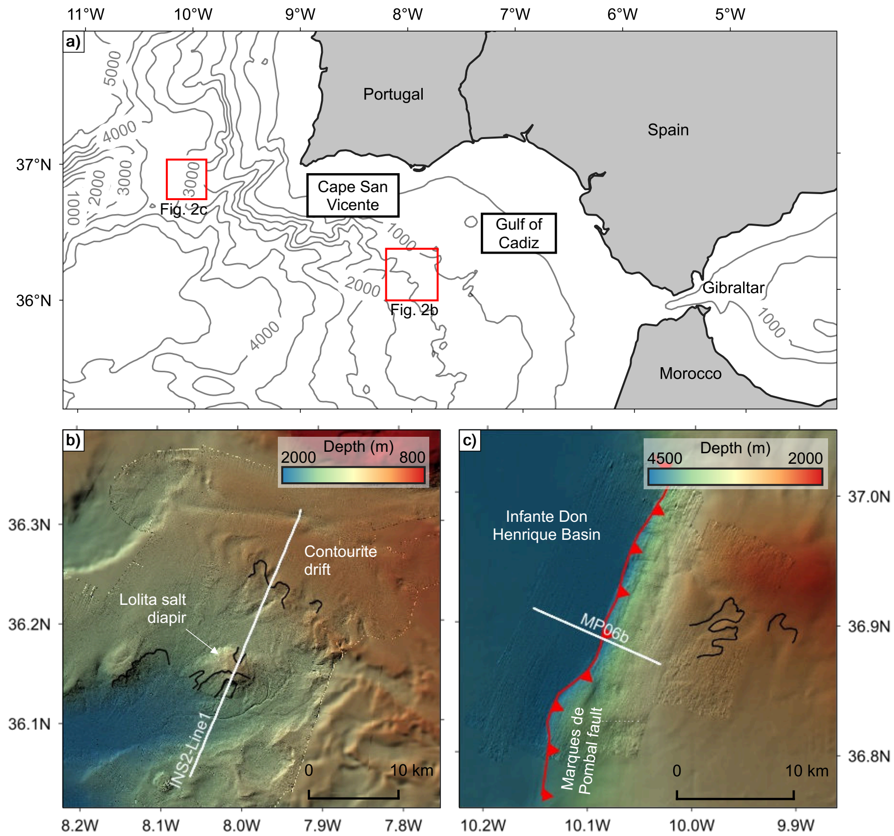

Figure 2. a) Overview map of the Gulf of Cadiz and surroundings, with bathymetric contours (500 m interval). b) Bathymetry of Portimão Bank area, location of seismic profile INS2-Line1 indicated. c) Bathymetry of Infante Don Henrique Basin area, location of Marquês de Pombal fault trace at the seafloor (after Gràcia, Dañobeitia, Vergés, & Team, 2003) and seismic profile MP06b indicated. Headscarps from mass-movements are shown as black lines.

Leynaud et al., 2017). This study uses geophysical data collected from two areas of the Gulf of Cadiz: the Portimão Bank and the Infante Don Henrique Basin.

The Portimão Bank is an east-west trending tectonic high located south of Portugal, at the external part of the Gulf of Cadiz. The area is characterised by bottom currents and contourite deposition associated with the Mediterranean Outflow Water (Brackenridge et al., 2013) and mass-movements (slides and slide scars; Silva et al., 2020). Salt diapirs pierce the shallow Plio-Quaternary sediments and the corresponding doming is evident in the bathymetry (Fig. 2b). The rapid deposition of poorly consolidated contourites and slope steepening from salt diapirism are primary pre-conditioning factors for mass-failure, evidence of which is widespread in the area (Mulder et al., 2009; Silva et al., 2020).

The Infante Don Henrique Basin is located at the south west of the Cape São Vicente (Fig. 2). It is bound on its eastern side by the Marquês de Pombal fault, a ∼55 km long, north-south trending, active reverse thrust fault (Gràcia, Dañobeitia, Vergés, Bartolomé, & Córdoba, 2003; Terrinha et al., 2003; Zitellini et al., 2004). The fault is expressed in the bathymetry as a monocline, with water depth rapidly increasing from the hanging-wall block (2000 m water depth) to the basin located in the footwall block (3900 m water depth). A succession of stacked MTCs is preserved in the Plio-Quaternary deposits in the basin, likely recording recent seismic activity of the fault (Vizcaino et al., 2006; Gràcia et al., 2010), which has been considered as a potential source of the $M_w > 8$ 1755 Lisbon earthquake (Baptista et al., 1998; Terrinha et al., 2003). Recent mass-failure events are also visible in the bathymetry of the steeply dipping hanging wall block (Fig. 2c). Preconditioning factors for mass-failure in the area include slope steepening of the advancing thrust front and potential excess pore pressure related to the relatively high sedimentation rate and lateral fluid flow. Near-field seismic activity along the Marquês de Pombal fault is likely a primary trigger mechanism for some of the mass-failure events, as well as far-field seismicity from the rest of the Gulf of Cadiz.

3 Data and Methods

3.1 Geophysical Data

This study uses two 2-D marine multi-channel seismic reflection profiles from the Gulf of Cadiz acquired during the INSIGHT (Imaging large seismogenic and tsunamigenic structures of the Gulf of Cadiz with ultra-high resolution technologies) cruises in May 2018 (Leg 1) and October 2019 (Leg 2) (Gràcia et al., 2018; Urgeles et al., 2019).

The seismic acquisition and processing flow were designed to maximise the temporal and spatial resolution of the resulting seismic images. The shot interval was chosen to ensure a nominal coverage of at least 12-fold with a midpoint interval of 3.125 m. A relatively small seismic source (an airgun array with total volume 930 cu. in.) was used to maximise the dominant source frequency. The source array and streamer were towed at a relatively shallow depth (∼3 m) to ensure that the frequency of the first source and receiver ghost notches were as high as possible. Broadband pre-processing was performed onboard using RadExPro seismic processing software. Traditional pre-processing focuses on imaging specular reflections, meaning that diffractions are often ignored or removed, particularly by processes that target dipping energy, such as $\tau-p$ and $f-k$ filters. Preserving diffractions through the pre-processing flow requires care as they are generally lower amplitude, higher frequency and dip more steeply compared to reflections. The broadband pre-processing flow consisted of i) swell noise removal (to enhance the signal-to-noise ratio at low frequencies); ii) deghosting (to correct for the source and receiver ghost effect, enhancing the bandwidth); iii) designature (to transform the data to zero-phase and remove the bubble pulse, boosting the low frequency content) and iv) shot domain $\tau-p$ muting (to remove steeply dipping noise, taking care to preserve the diffractions). For most of the survey area the signal penetration depth was similar to, or less than, the two-way travel time (TWTT) of the first waterbottom multiple, therefore no multiple attenuation was performed. Instead, a bottom-mute was applied from above the first waterbottom multiple before imaging to prevent high amplitude multiple energy from migrating upwards into the shallow section as noise. Full details of the acquisition and pre-processing parameters for both profiles are given in the supplementary information (Table S1 and Table S2). The signal bandwidth of the migrated full-wavefield images is approximately 8 Hz to 250 Hz (range estimated from the amplitude spectrum of a window around the waterbottom reflection, 20 dB below the peak amplitude).

3.2 Diffraction Separation

This study uses a dip-guided plane-wave destruction (PWD) filter approach for diffraction separation on unmigrated data, modified to be robust to high amplitude diffractions and steeply dipping reflections present in the example profiles from the Gulf of Cadiz.

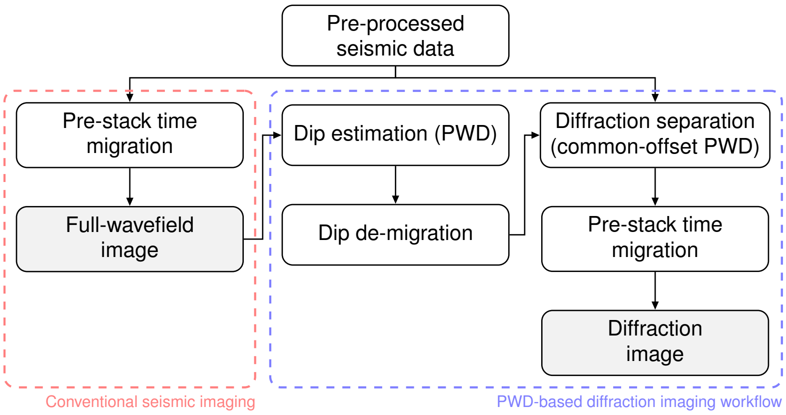

Figure 3. Comparison of workflows for conventional full-wavefield seismic imaging and the plane-wave destruction (PWD) filter based diffraction separation and imaging workflow used in this study. The dip field is estimated from the migrated full-wavefield image, then de-migrated using the migration velocities, giving the dominant slope of the unmigrated reflections (Appendix A). This is used to guide the PWD filter for diffraction separation.

Fig. 3 shows an outline of the diffraction imaging workflow compared to a conventional full-wavefield seismic imaging workflow.

The recorded seismic wavefield can be considered as the superposition of i) reflected energy, ii) diffracted energy and iii) noise (including other seismic arrivals, such as multiples). When the noise is low, the diffracted wavefield can be retrieved by subtracting the reflected wavefield from the recorded wavefield. In this study we perform the separation using a dip-guided PWD filter approach in the time domain on common-offset gathers (as in, e.g., Fomel et al., 2007; Decker et al., 2017). This approach assumes that reflections are locally planar events in common-offset domain (Harlan et al., 1984). PWD filters calculate the dominant local slope by following energy between traces and iteratively minimising the residual energy (Claerbout, 1992; Fomel, 2002). The residual energy contains the diffracted energy and noise, with laterally coherent events with continuous local slope (i.e., smooth) that are close to the estimated dominant slope (the apparent dip of the unmigrated reflectors) eliminated.

The PWD filter is guided by an estimate of the dominant slope (dip). Robust diffraction separation therefore depends on accurate estimation of the dominant slope of the *unmigrated* reflections. Due to the general rough topography of the seafloor in the Gulf of Cadiz, the example profiles in this study contain a large number of high energy diffractions with similar amplitude to major reflections. In addition, some reflections are steeply dipping, often sub-parallel to the diffraction tails. This prevents accurate estimation of the dominant slope of the reflectors directly from the unmigrated data (as in, e.g, Fomel et al., 2007). We instead estimate the dip field from the migrated full-wavefield image, where diffractions are collapsed and the continuity of reflections enhanced. Using the migration velocities, we then de-migrate this dip field to estimate the dominant slope of the unmigrated reflections. Details of the dip de-migration algorithm are given in Appendix A.

3.3 Imaging

Diffractions, like reflections, can be imaged by Kirchhoff-type migrations, in both time and depth domains (Moser & Howard, 2008). For this study, the real data examples are migrated using a 2-D pre-stack Kirchhoff time migration (Lumley et al., 1994; Fomel et al., 2013), with a migration aperture limited to 60°. Identical migrations are performed for the full-wavefield and diffraction images so that the geometry of both images is comparable (Fig. 3). The diffraction images in this study are presented as the energy (squared envelope) of the diffraction image (as in, e.g., Preine et al., 2020).

A classic application for diffraction imaging is to derive migration velocity fields by focusing analysis of the diffracted wavefield (e.g., Fomel et al., 2007; Decker et al., 2017; Preine et al., 2020). Under the correct migration velocity, diffractions will collapse (focus) to a point at their apex. The example 2-D profiles in this study both contain significant contributions from out-of-plane diffractions around the target MTCs and from the rugose seafloor (Section 3.4). Out-of-plane diffractions will not be properly focused by 2-D migration, so their presence biases the derived migration velocity fields. As a consequence, we were not able to obtain plausible migration velocities from focusing-defocusing analysis of the diffracted wavefield in these examples. A more traditional method for migration velocity analysis is to pick velocity trends from semblance panels of migrated common-midpoint gathers. This method relies on the approximately hyperbolic moveout of seismic reflections with offset. The example 2-D profiles in this study were acquired with a relatively short streamer, giving a low far-offset (hundreds of metres) with respect to the depth of the target MTCs (kilometres). Consequently, there was not great enough differential moveout between reflections to perform an accurate and robust semblance velocity analysis.

Instead, the migration velocity fields used in this study were derived during onboard processing as a constant velocity in the water column and a velocity gradient in the sediments. The post-migration waterbottom horizon was picked on a near-offset section migrated with a water velocity Stolt migration (Stolt, 1978). The optimal sediment velocity gradients were estimated for each area by generating an ensemble of images migrated with a range of gradients and choosing the gradient that appeared to best focus reflections and diffractions for all profiles in an area. The sediment velocity gradient is then inserted below the smoothed post-migration waterbottom horizon to make the migration velocity field. For seismic profiles INS2-Line1 and MP06b the optimal sediment velocity gradient was estimated during onboard processing as $200\,\mathrm{ms^{-2}}$ and $125\,\mathrm{ms^{-2}}$, respectively (Gràcia et al., 2018; Urgeles et al., 2019). The water velocity for both profiles is $1500\,\mathrm{ms^{-1}}$. The resulting migration velocity fields are presented in the supplementary information (Fig. S5). These migration velocities are considered reasonable at the target depths because the MTCs in these examples are close to the seafloor (with respect to the water depth) and both the reflection and diffraction images appear to be generally well-focused. A sensitivity analysis of the diffraction imaging to changing the migration velocities is presented in the supplementary information (Fig. S7).

3.4 Constraining the Location of Out-of-Plane Diffractors

For 2-D seismic profiles, out-of-plane energy (i.e., seismic energy reflected and scattered from interfaces outside the vertical plane of the profile) can contaminate the image. The illumination of seismic reflectors depends on the local dip of the reflector and the geometry of the receiver array. Diffractions, however, are 3-D phenomena, fully illuminated from all angles even by single-channel, zero-offset data (Fig. 1a, Preine et al., 2020). This means that 2-D diffraction images will suffer more strongly from out-of-plane energy than corresponding 2-D reflection images. Out-of-plane energy is usually regarded as a source of noise in 2-D seismic profiles, as it cannot be properly migrated and interferes with in-plane primary energy.

We suggest that these out-of-plane diffractions, under certain strong assumptions, may provide a source of information about the 3-D geometry of MTCs from 2-D profiles. MTCs are inherently 3-D geobodies (Fig. 1b), so 2-D seismic images of MTCs will, in general, suffer more strongly from out-of-plane energy than 2-D seismic images of unfailed sediments. Therefore we expect *diffraction images* of MTCs from 2-D seismic profiles to contain particularly large contributions from out-of-plane energy.

The apparent TWTT of an out-of-plane diffractor, t_{diffr}, can be predicted from the cross-line distance to the diffractor, x, the depth of the diffractor below the seismic datum, z, and the average velocity along the raypath from the seismic array to the diffractor, v_{rms} (Fig. 4):

$$t_{diffr} = \frac{2\sqrt{x^2 + z^2}}{v_{rms}}. \tag{1}$$

If diffractors are distributed throughout the MTC, some of the recorded diffraction energy will always come from *outside* the vertical plane of the profile (i.e., $|x| > 0$ in Fig. 4). If the body is wider than it is thick and contains abundant diffractors, the apparent thickness of the slide from diffraction images will be greater than the apparent thickness of the slide from reflection images. This results in a "shadow" of diffraction energy below the true basal surface of the MTC in 2-D diffraction images. From Eq. 1 it follows that the thickness of this *diffraction shadow* is related to the half-width, perpendicular to the profile, of the zone of out-of-plane diffractors that contribute to the image. We propose that this could provide a minimum bound on the cross-line half-width of an MTC (i.e., relate the zone where out-of-plane diffractions could potentially come from to the geometry of an MTC) under certain (strong) assumptions:

Diffractors spread throughout body Diffractors are widespread inside the body compared to outside the body, where there are relatively fewer diffractors.

Known top surface The top surface of the MTC must be assumed. In practice, this can often be well-constrained by bathymetry (for bodies at the seafloor) or reasonably assumed to be constant depth perpendicular to the profile.

Thin body The thickness of the body is small relative to its depth, meaning that all diffractors can be treated as if they are at the assumed top surface.

Laterally homogeneous overburden velocity Eq. 1 assumes a straight raypath to the true location of the diffractor, implying that the overburden velocity, v_{rms}, is constant in a cross-line direction, even if the water depth changes.

Distinct diffraction shadow The diffraction shadow is associated with a single body and can be clearly differentiated from the background and from other bodies that

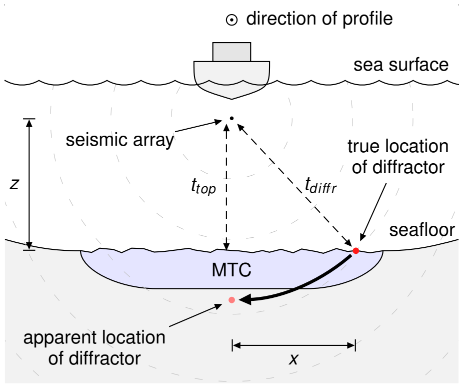

Figure 4. Conceptual diagram oriented perpendicular to a 2-D seismic profile showing how an out-of-plane diffractor at the seafloor will appear to "swing" into the plane of the profile. The seismic source and receiver arrays (seismic datum) and the expanding seismic wavefront are marked. x and z are the the horizontal offset and depth of the diffractor with respect to the seismic array. t_{top} and t_{diffr} are the two-way travel times to the top of the MTC and to the diffractor.

might also generate diffractions. The cross-line width is large enough with respect to the thickness that the diffraction shadow extends *below* the true basal reflector.

If these assumptions are satisfied, the diffraction shadow provides an estimate of the half-width of the zone containing the diffractors that swing into the profile. In other words, it places a lower bound on the width of an MTC from a single 2-D seismic profile. Diffractions are relatively low amplitude seismic events, and their radiation pattern means that their amplitude depends strongly on the distance from the seismic array (Fig. 1a). Therefore this lower bound on the half-width from the diffraction shadow will generally be an underestimate of the true half-width, in practice.

3.4.1 Controlled Synthetic Demonstration

The aim of this synthetic test is to demonstrate that 3-D information generated by a heterogeneous geobody is encoded in 2-D seismic profiles by out-of-plane diffractions, producing a diffraction shadow. If the above assumptions are satisfied, the apparent TWTT to the base of the diffraction shadow can be related to the overall width of the geobody by Eq. 1.

The 3-D synthetic model has dimensions 500 m x 500 m x 500 m with a grid spacing of 1 m. The P-wave velocity is constant, $v_p = 1500\,\mathrm{m\,s^{-1}}$. The background density is constant, $\rho = 1400\,\mathrm{kg\,m^{-3}}$, everywhere except for a half-ellipsoidal region, representing an MTC, in the centre of the model. Inside the half-ellipsoid zone are randomly located $n = 2117$ point diffractors (single cells of higher density, $\rho = 3000\,\mathrm{kg\,m^{-3}}$). The 3-D, zero-offset seismic response is modelled using one-way wave extrapolation with an extended split-step scheme (Gazdag & Sguazzero, 1984; Kessinger, 1992) and a 50 Hz Ricker wavelet source signature. The modelled seismic volume, 3-D migration and 2-D migration of a section through the diffractor zone are presented in Section 4.4.1.

3.4.2 Real Data Demonstration

The aim of this real data test is to demonstrate a practical workflow to assess the zone of out-of-plane diffractors that contribute to example seismic profile INS2-Line1. As MTC A is close to the seafloor we can make the simplifying assumption that potential internal diffractors are at, or near, the seafloor (Section 3.3). This implies $v_{rms} \approx v_{water} = 1500\,\mathrm{m\,s^{-1}}$. We also assume that the seafloor is equivalent to the potential top surface of the MTC. The seafloor depth is known independently from multi-beam swath bathymetry (Fig. 2).

The workflow to calculate the zone of diffractors that contribute to the image is as follows:

1. Pick the apparent base of the diffraction shadow associated with the MTC, t_{diffr}, from the diffraction image.
2. For each interpreted common-midpoint (CMP) location along the profile:

   (a) Compute the horizontal distance, x, from the CMP to each point on the seafloor.

   (b) For each point on the seafloor, compute the TWTT from the CMP to the potential top surface of the body, t_{top}, using Eq. 1 with $v_{rms} = 1500\,\mathrm{m\,s^{-1}}$ and z equal to the depth of the seafloor.

   (c) Grid points with TWTT less than the interpreted base diffraction shadow ($t_{top} < t_{diffr}$) are considered as potential locations for diffractors originating perpendicular to the profile at this CMP location.

4 Results

4.1 Diffraction Imaging

4.1.1 Profile INS2-Line1

The full-wavefield seismic image of the INS2-Line1 profile largely consists of parallel, high amplitude reflectors interpreted to be of Plio-Quaternary age, pierced by the Lolita salt diapir, forming a dome at the seafloor ∼4 km wide in the centre of the profile (Fig. 5). The doming has resulted in slope failures that radiate from the centre of the dome, visible in the bathymetry (Fig. 2b). To the north, the upper Late Quaternary sediments onlap and pinchout, which characterises a major contourite drift deposit resulting from bottom currents associated with the Mediterranean Outflow Water. Three prominent MTCs, MTC A, MTC B and MTC C are clearly visible on the full-wavefield seismic image (Fig. 5a and Fig. 6a, a zoom on MTC A). MTC A and MTC B are both exposed at the seafloor, having in-profile lengths of ∼7.4 km and ∼3.7 km, respectively, and maximum in-profile thicknesses of ∼95 ms TWTT and ∼130 ms TWTT, respectively. MTC C is deeper, partly underlying MTC B, with an in-profile length of ∼5.1 km and a maximum in-profile thickness of ∼140 ms. MTC A originated from the drift deposits, whereas MTC B originated from the salt diapir. Both propagated towards the south. MTC C, instead, failed towards the north, in the direction of the salt diapir.

Fig. 5b shows the unmigrated full-wavefield stack of INS2-Line1. Diffraction tails are visible originating from the rugose, high amplitude seafloor and top salt interfaces. Fig. 5c shows the estimated dominant slope of the unmigrated reflectors (de-migrated dip field estimated from the full-wavefield seismic image) overlaid on the unmigrated stack. The dip estimate appears to follow the dip of the prominent horizons well.

Fig. 5d shows a stack of the separated diffractions. This view is comparable to the unmigrated stack (Fig. 5b). Diffraction tails are clearly seen throughout the section, including from i) two zones of normal faults (CMPs 1500 to 3000 and 9100 to 10 000); ii) inside the prominent MTCs (CMPs 3000 to 5500 and 7000 to 9000) and iii) within the deeper, chaotic unit (CMPs 1000 to 5000 and 9000 to 10 000, below around 2.4 s). The diffraction image shows high amplitudes inside MTC A, MTC B and MTC C, inside the smaller MTC D (below MTC A), at the rugose top salt interface and within the deeper chaotic unit (Fig. 5e). Both zones of normal faults are remarkably well-resolved compared

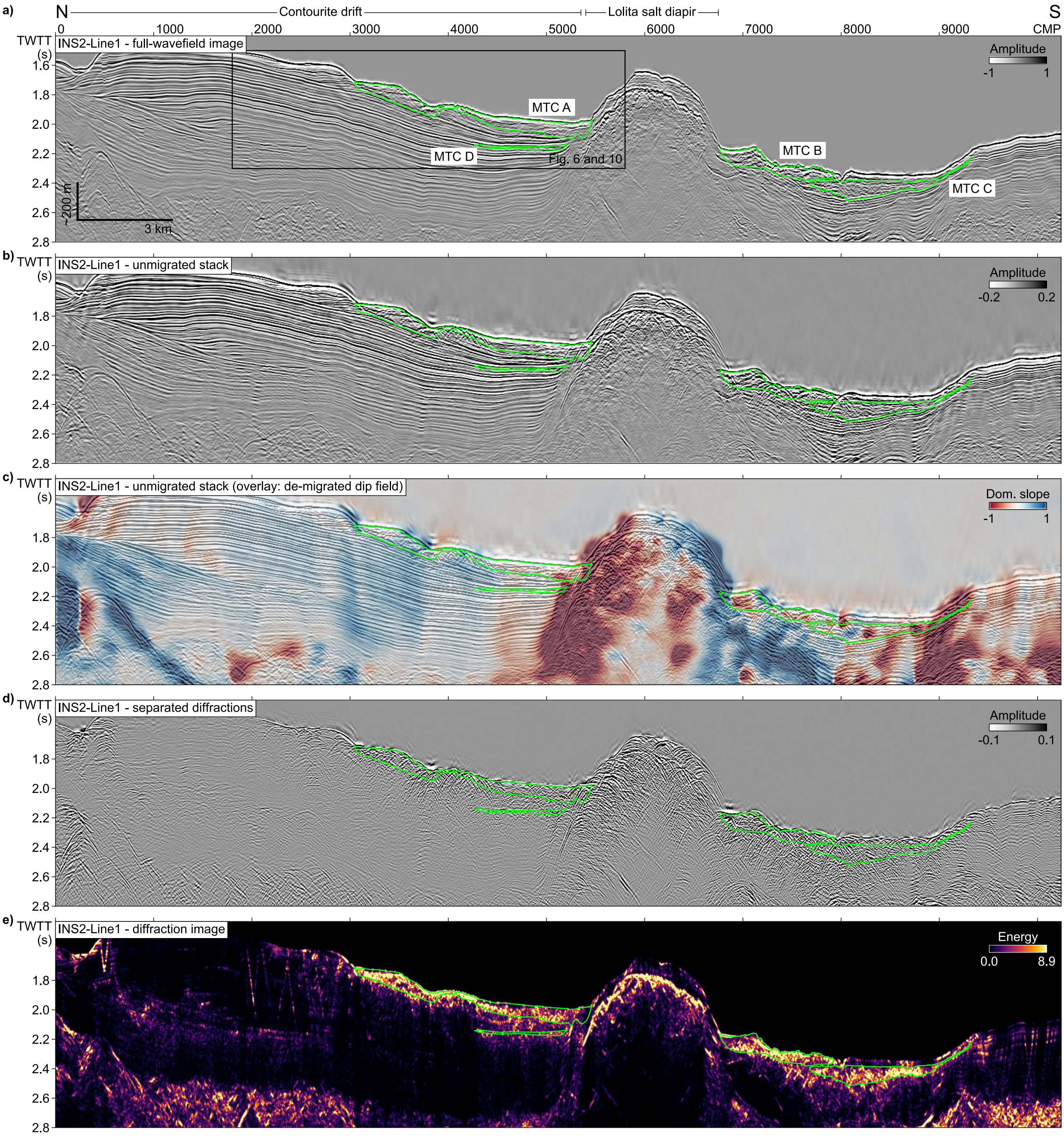

Figure 5. Seismic profile INS2-Line1 from the Portimão Bank area (Fig. 2), MTCs outlined in green. a) Full-wavefield migrated seismic image. b) Unmigrated stacked conventional data (reflections and diffractions). c) De-migrated estimated dip field (dominant slope of reflectors) overlaid on the unmigrated conventional stack. d) Unmigrated stacked separated diffractions. e) Diffraction image.

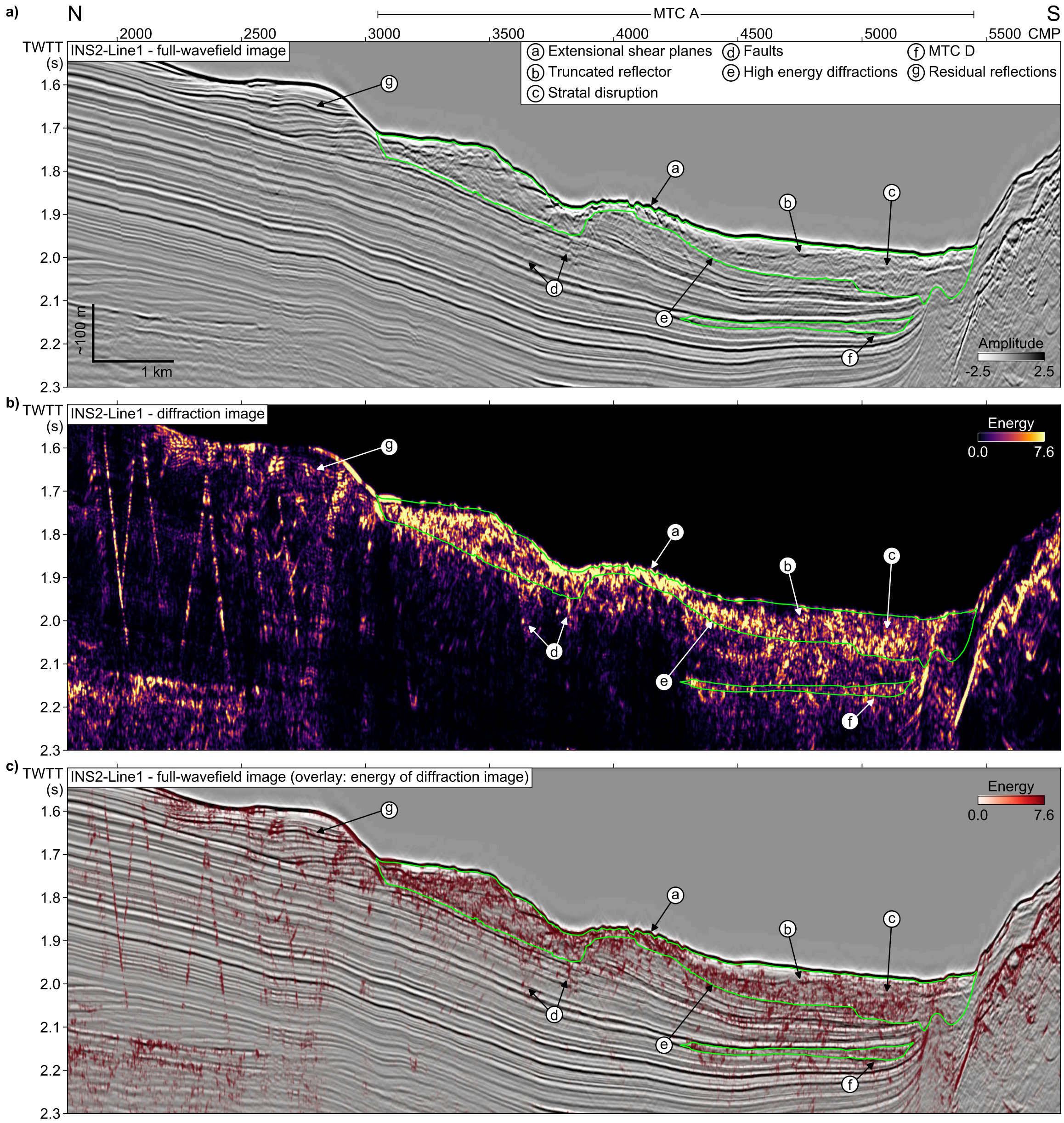

Figure 6. A section of seismic profile INS2-Line1 (Fig. 5) from the Portimão Bank area containing a prominent MTC. Speculative interpreted structure is labelled. a) Full-wavefield seismic image, migrated reflections and diffractions. b) Diffraction image, migrated diffractions. c) Energy of the diffraction image overlaid on the full-wavefield image, to highlight location of diffractors.

to in the full-wavefield image, where they are difficult to interpret due to their small offsets. Some residual reflection energy remains, particularly in areas of rapidly varying dip (see Fig. 6, label "g").

4.1.2 Profile MP06b

The MP06b seismic profile is a cross-sectional view of the Marquês de Pombal fault (Figs. 7 and 8). The profile can be divided into two main sections: the Infante Don Henrique Basin (the footwall of the Marquês de Pombal fault) and the steeply dipping slope area (the frontal part of the hanging wall of the fault). The full-wavefield seismic image shows that the Infante Don Henrique Basin contains a >1 s TWTT thick, stacked succession of MTCs with apparently chaotic to transparent seismic character, separated by parallel horizons representing the unfailed confining sediments (Fig. 7a and Fig. 8a). The hanging wall of the Marquês de Pombal fault is more deformed—the shallow part of the slope shows extremely disordered, overlapping horizons reflecting the complex seafloor topography caused by mass-wasting in the slope area. The Marquês de Pombal fault plane is not directly imaged in this data; the fault zone is represented by a zone of relatively low amplitude, disordered reflectors, dipping to the south east (CMPs 1900 to 2500, 5.25 s to 6.5 s TWTT).

Fig. 7b shows the unmigrated stack of MP06b. Diffraction tails are visible originating from the rugose seafloor in the steeply dipping hanging wall area (CDPs 1800 to 3000) and from truncated reflectors where the Infante Don Henrique Basin meets the low amplitude, disordered zone containing the Marquês de Pombal fault. Fig. 7c shows the estimated dominant slope (de-migrated dip field estimated from Fig. 7a) overlaid on the unmigrated stack. In general, the dominant slope appears to follow the dip of the prominent horizons well, showing near-zero slope in the Infante Don Henrique Basin and negative slope (i.e., dipping to the north west) in the hanging wall area. The south eastern, deep corner of the profile (CMPs >2500, >5.5 s TWTT) shows anomalously high slope values corresponding to steeply dipping noise, due the to low signal-to-noise ratio in this part of the image. Fig. 7d shows a stack of the separated diffractions, where diffraction tails are seen throughout, particularly from disrupted reflectors in the hanging wall area (CMPs 2000 to 4200) and corresponding to MTCs in the Infante Don Henrique Basin (CMPs 0 to 2000, 5.2 s to 6 s TWTT). Fig. 7e shows the diffraction image (i.e., the separated diffractions after migration), which contains laterally continuous, high amplitude

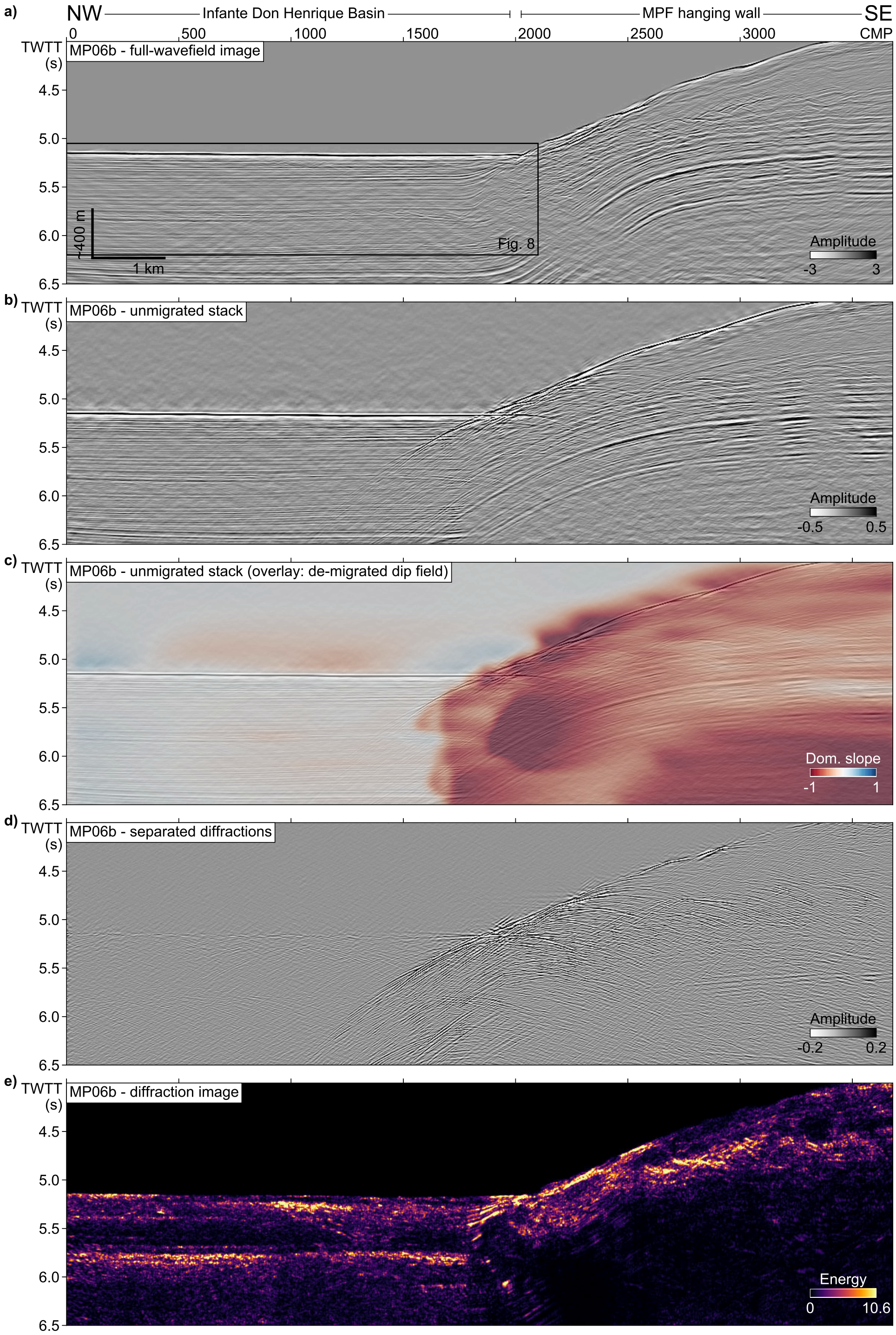

Figure 7. Seismic profile MP06b from the Marquês de Pombal fault zone area (Fig. 2). The Marquês de Pombal fault (MPF) is located around CMP 2000. a) Full-wavefield migrated seismic image. b) Unmigrated stacked full-wavefield data. c) De-migrated estimated dip field (dominant slope of reflectors) overlaid on the unmigrated full-wavefield stack. d) Unmigrated stacked separated diffractions. e) Diffraction image.

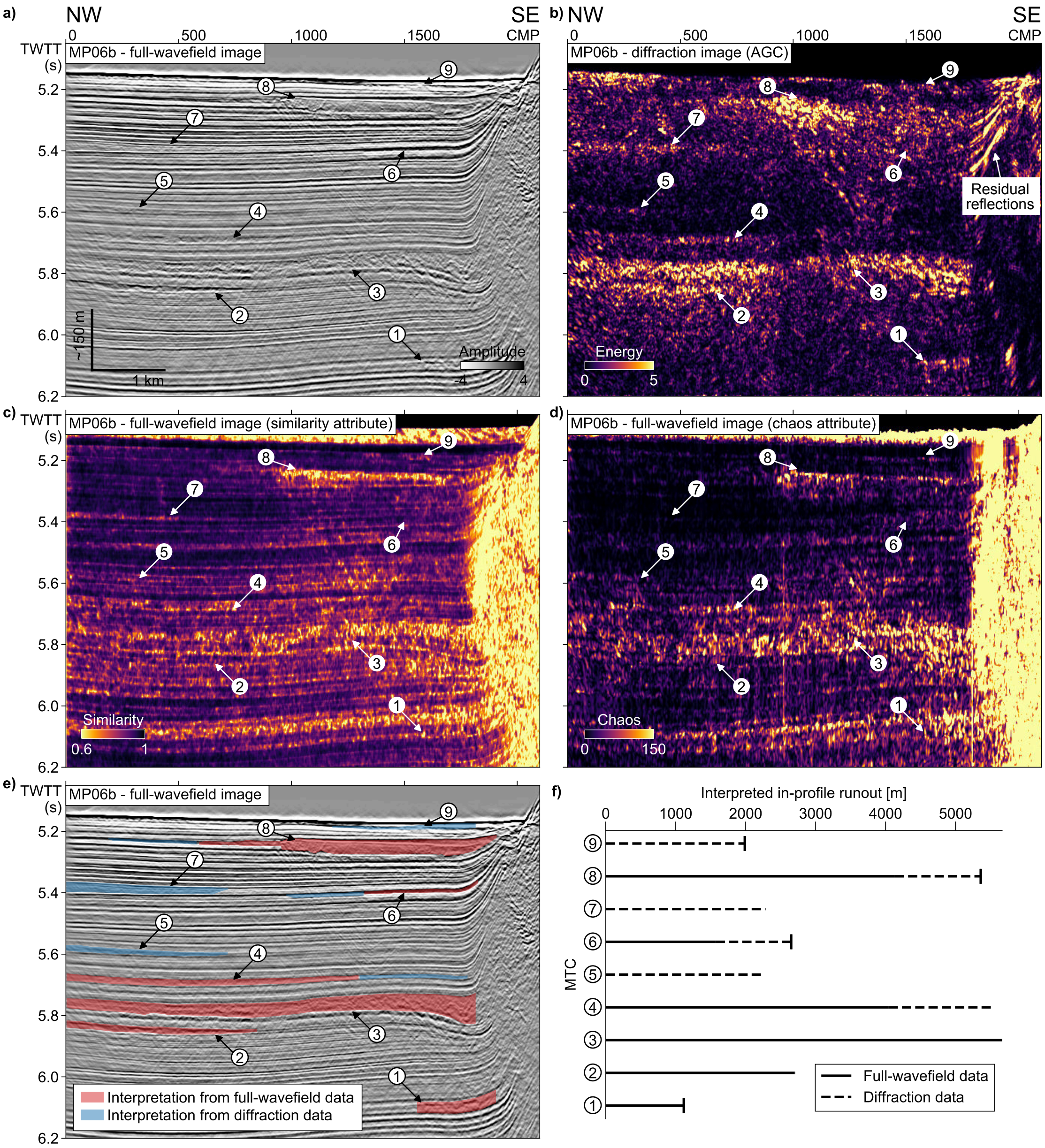

Figure 8. A section of seismic profile MP06b from the Marquês de Pombal fault area (Fig. 7). Interpreted MTCs are labelled from 1 to 9. a) Conventional full-wavefield seismic image. b) Diffraction image. c) The similarity attribute and d) the chaos attribute derived from the full-wavefield seismic image. e) The interpreted MTCs overlaid on the full-wavefield image. The extent of the bodies interpretable from the full-wavefield images and attributes is shaded red, the (extra) extent interpretable from the diffraction image is shaded blue. f) The proportion of the apparent in-profile runout length of each body interpreted from the full-wavefield image and attributes, compared to that interpreted also using the diffraction image.

zones that correspond to MTCs seen in the full-wavefield seismic image. Some residual reflection energy remains, particularly in the area of rapidly varying dip at the break in slope corresponding to the Marquês de Pombal fault (CDP 2000, see Fig. 8b).

4.2 Comparison of Full-Wavefield and Diffraction Images of Internal Structure

Fig. 6 shows a section of seismic profile INS2-Line1 around MTC A, exposed at the seafloor (Fig. 5), including the full-wavefield seismic image (Fig. 6a), the corresponding diffraction image (Fig. 6b) and the diffraction image overlaid on the full-wavefield image (Fig. 6c). MTC A is characterised by relatively high amplitude response in the diffraction image, whereas the unfailed underlying sediments are characterised by a relatively low amplitude response. This implies that MTC A contains a relatively high density of diffractors compared to the unfailed sediments. We speculate that these high amplitude diffractions could result from: (a) faults or shear planes in an extensional part of the MTC; (b) a truncated internal reflector within the MTC; (c) a zone of intense stratal disruption within the MTC (possibly the interface between two separate mass-transport deposits); (d) two small normal faults directly beneath the MTC, likely related to sediment loading/unloading after failure; (e) a zone of diffuse, high energy diffractors that is not clearly related to structure resolved by the full-wavefield image and (f) a smaller, deeper MTC (MTC D). The remaining diffraction energy within the MTC has complex geometry and is not clearly related to structure resolved by the full-wavefield image (e.g., the area labelled “e”).

4.3 Comparison of Diffraction Image with Discontinuity Attributes

Fig. 8 shows a section of seismic profile MP06b, focused on the stacked succession of MTCs in the Infante Don Henrique Basin. Fig. 8a shows the full-wavefield seismic image, Fig. 8c shows the similarity attribute of the full-wavefield image (similarity attribute implementation from OpendTect 6.4 with a time gate of 10 ms) and Fig. 8d shows the chaos attribute of the full-wavefield image (“Chaotic Reflection” attribute implementation from Kingdom Rock Solid Attributes). Fig. 8b shows the corresponding diffraction image. In general, the diffraction image appears to have lower noise and less interference from high amplitude reflections than the discontinuity attributes of the full-wavefield image. There is a prominent zone of residual reflection energy at the break in slope across the Marquês de Pombal fault (labelled). In addition, a steeply dipping event cuts across part of the image from CMPs 800 to 1250, 5.2 s to 5.6 s TWTT (seen also on the full-wavefield image and discontinuity attributes). We interpret this event as out-of-plane energy associated with MTC8, as it appears to originate from the edge of the thickest part of this body.

Interpretation of the MTCs is guided by one or more of the following features: i) apparently chaotic or transparent seismic character in the full-wavefield seismic image; ii) high amplitude, laterally continuous top and/or basal bounding reflections; iii) lobe shaped, laterally consistent low similarity/high chaos values or iv) lobe shaped, laterally consistent high amplitude diffraction energy. In total, nine MTCs are interpreted from a combination of the full-wavefield image, derived attributes and the diffraction image (labelled in order of decreasing depth from MTC1 to MTC9). Three large bodies are directly visible in the full-wavefield seismic image (MTC3, MTC4 and MTC8). Two other bodies are only resolved by the diffraction image (MTC5 and MTC7). A further zone of high amplitude diffractions close to the seafloor (CMPs 0 to 400, 5.15 s TWTT) is not interpreted as an MTC as the zone cuts across apparently parallel, undisturbed reflectors. We speculate that this diffraction energy could be from out-of-plane or generated by rough seafloor topography.

Fig. 8e shows the interpreted lateral extent and thickness of the interpreted bodies overlaid on the full-wavefield seismic image. The portion of the bodies interpreted from the full-wavefield image and attributes versus the diffraction image is indicated. Fig. 8f shows the interpreted length (apparent in-profile runout) of these bodies, indicating the proportion of the total length interpretable only from the diffraction products. Several of the bodies (MTC2, MTC3, MTC4, MTC5 and MTC7) extend past the end of the section, in these cases the interpreted runout length is a lower bound on their total runout length in the direction of the profile. MTC4 and MTC6 are both resolved from the full-wavefield products, but by using the diffraction image their in-profile runout length is extended by >1.5 km and 1.1 km respectively. MTC7 is only resolved by the diffraction image, likely because it has an apparently transparent seismic character in the full-wavefield seismic image, whereas the diffraction image clearly resolves a lobe shaped zone of heterogeneity. MTC9 is a 2 km long body near the seafloor that is only visible in the diffraction image, likely because it is thin enough to be masked in the full-wavefield seismic image by the relatively high amplitude, long wavelength seismic reflections.

4.4 Constraining the Location of Out-of-Plane Diffractors

4.4.1 Controlled Synthetic Demonstration

Fig. 9 shows the results of the controlled synthetic demonstration of the "diffraction shadow" concept. This demonstration models an MTC body as a half-ellipsoid containing randomly placed point diffractors. Fig. 9a shows the top and base boundaries of the body and the point diffractors (single cell density anomalies). Fig. 9b shows the forward modelled, zero-offset volume in time domain. As the model is composed entirely of diffractors (no reflections), this is equivalent to the ideal separated diffracted wavefield. Fig. 9c shows the zero-offset volume after migration with a 3-D constant velocity ($v_p = 1500\,\mathrm{m\,s^{-1}}$) Stolt migration (Stolt, 1978), giving an idealised diffraction-only image. The diffractions are properly focused back to their apexes, which lie within the boundaries of the body (converted to TWTT). Some energy lies slightly outside these boundaries, due to the band-limited, zero-phase source wavelet. Fig. 9d shows a single 2-D section of the volume at $y = 250\,\mathrm{m}$, migrated with an equivalent 2-D constant velocity Stolt migration. Out-of-plane diffracted energy is not properly imaged by the 2-D migration. The result is a generally chaotic internal seismic character within the body (compare to Fig. 9c) and a diffraction shadow that extends beneath the body with a maximum thickness of $\sim$20 ms. The extent of the diffraction shadow agrees well with the predicted maximum extent based on the width of the body and Eq. 1.

4.4.2 Real data application

Figs. 10a and 10b show the true basal surface of MTC A picked from the full-wavefield seismic image (INS2-Line1), alongside the picked base of the diffraction shadow, the limit of diffractions interpreted to be associated with MTC A. Fig. 10c shows the lateral extent and thickness of MTC A, interpreted from a combination of multi-channel seismic and sub-bottom profiler lines and the bathymetry, giving a total volume of $5.5\,\mathrm{km^3}$ (converted from time to depth using the sediment velocity gradient of $200\,\mathrm{ms^{-2}}$). The methodology, multi-channel seismic profiles and an example of one of the sub-bottom profiles are presented in the supplementary information (Text S2 and Figs. S1-S4). Fig. 10d shows the TWTT contour to the potential top surface of MTC A (the seafloor) from seismic profile INS2-Line1 (calculated using Eq. 1), with the TWTT of the base diffraction shadow overlaid (magenta hatched area). This area shows the zone, perpendicular to the pro-

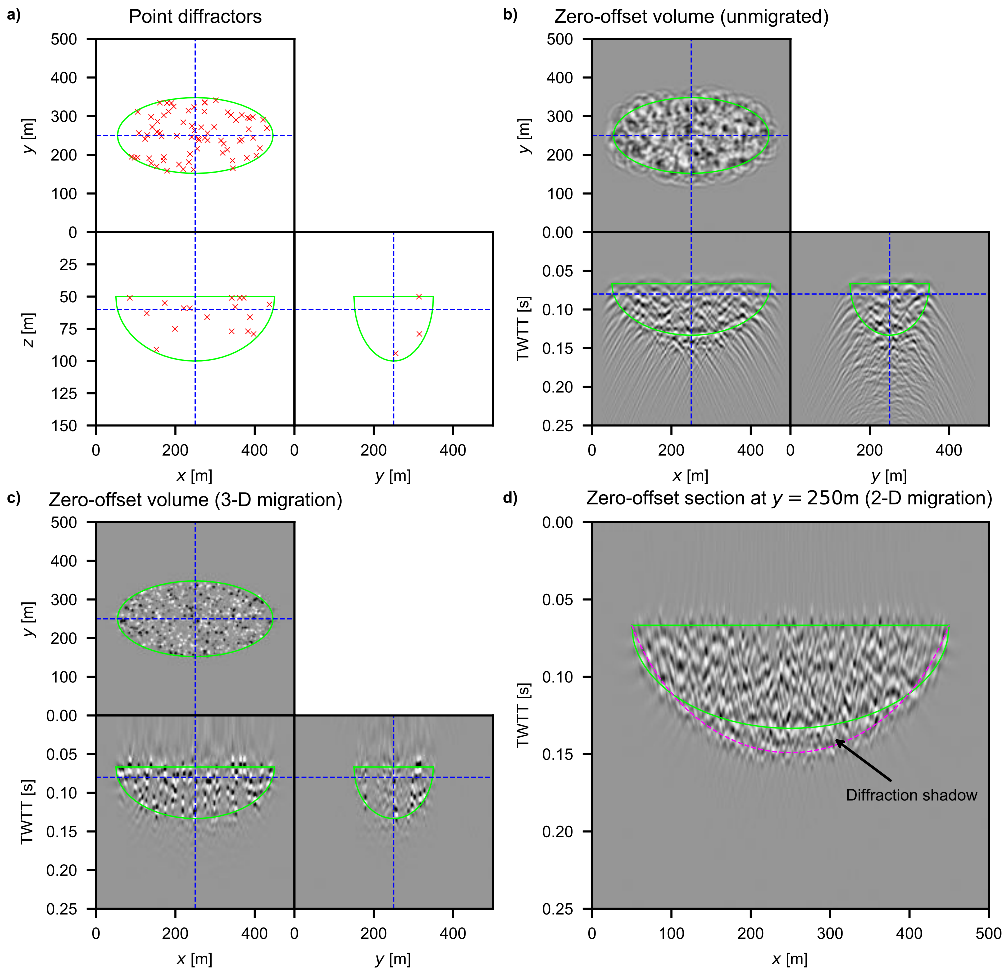

Figure 9. Controlled synthetic demonstration model setup and results. The boundaries of the half-ellipsoidal zone representing an MTC are outlined in green. a) 3-D model definition showing location of point diffractors (single-cell density anomalies) randomly placed within the MTC zone. b) 3-D forward modelled zero-offset volume. c) 3-D Stolt migration of (b). d) 2-D Stolt migration of a 2-D slice of (b) at $y = 250$. The base of the diffraction shadow predicted by Eq. 1 is shown in dashed magenta.

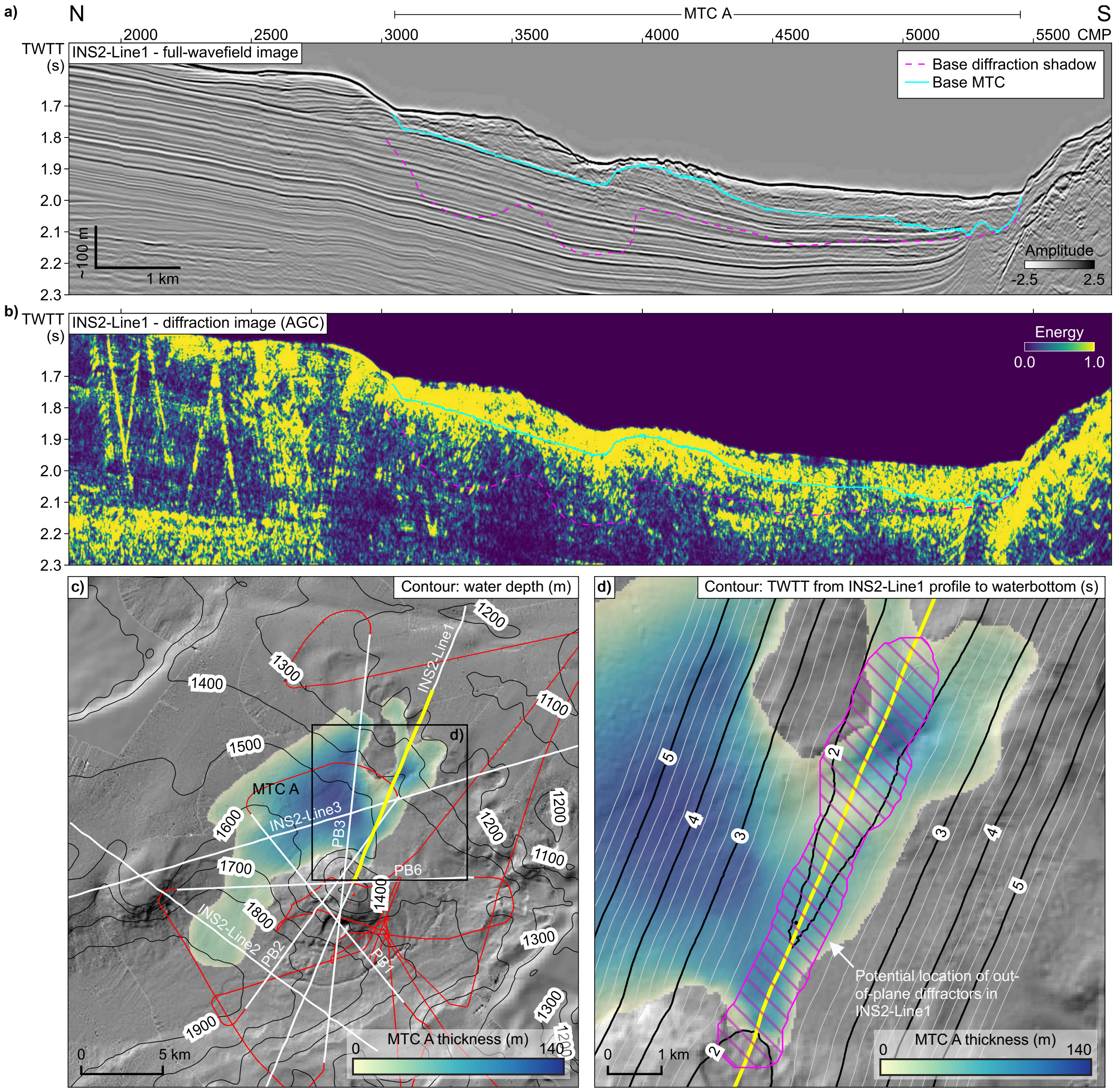

Figure 10. A section of seismic profile INS2-Line1 (Fig. 5) containing MTC A. a) The full-wavefield seismic image. b) The corresponding diffraction image, with interpreted basal surface from the full-wavefield image (solid blue) and interpreted base of the out-of-plane diffractions associated with MTC A (the diffraction shadow, dashed magenta). c) Water depth (contours) on the shaded relief of the area surrounding the Lolita salt diapir. The extent and thickness of MTC A is interpreted from the bathymetry, sub-bottom profiler data (red) and a network of multi-channel seismic profiles (white). d) Contour lines show the two-way travel time (TWTT) calculated from seismic datum to the seafloor (potential top MTC A surface) at each CMP location, perpendicular to the profile (Section 3.4.2). The hatched magenta area indicates the zone of potential locations for the out-of-plane diffractors implied by the base diffraction shadow pick in (a) and (b).

file, of the potential locations of diffractors that could contribute to the diffraction shadow associated with MTC A. The half-width varies from a minimum of ∼400 m to a maximum of ∼900 m, implying that diffraction energy from at least 900 m from the vertical plane of the profile has contributed to the image.

5 Discussion

5.1 Imaging Internal Structure

The diffraction image for profile INS2-Line1 (Fig. 6) clearly images a zone of normal faults between CMPs 1800 to 3000 and the rugose top salt interface of the Lolita salt diapir—both classic targets for diffraction imaging. The zone of normal faults, in particular, appears significantly better resolved compared to the full-wavefield image, where their small offset means they are barely visible. There is also a significantly higher concentration of diffraction energy within MTC A compared to the surrounding unfailed sediments. This suggests that the internal structure of MTC A contains significantly more wavelength and sub-wavelength scale discontinuities compared to the unfailed sediments, which can already be seen from the full-wavefield seismic image. This is consistent with outcrop examples of MTCs, which show that complex metre-scale internal structure can be preserved (Lucente & Pini, 2003). We observe high amplitude diffractors that coincide with structure observed on the reflection image related to MTC A: headscarp faults, truncated internal interfaces and strong stratal disruption. This is the type of small-scale (i.e., potentially sub-wavelength) geological heterogeneity that we would expect to generate diffractions (Fig. 1).

Diffractors that do not coincide with structure seen in the full-wavefield seismic image are also resolved (labelled “e” in Fig. 6). In the absence of high-resolution data, such as cores or sub-bottom profiler images, it is not clear exactly what type of structure these diffractors represent; we speculate that they may be related to small-scale internal structure that is also not well imaged by the full-wavefield image, such as local shear zones, intact embedded blocks or fluid escape features. Diffractions require both lateral heterogeneity (around or below the scale of the seismic wavelength) *and* an impedance contrast, so the presence of diffractions within a body is evidence that significant wavelength-scale (i.e, metre to decametre) internal structure is preserved after transport or generated during emplacement. Diffraction images can thus provide information on the degree of internal disaggregation or organisation by quantifying the degree of geological heterogeneity at scales close to the seismic resolution. High diffraction density within an MTC is likely to be associated with relatively low disaggregation, as it implies that wavelength-scale internal structure is preserved. Conversely, low diffraction density within an MTC could imply significant disaggregation—the scale of internal structure has been reduced to much lower than the seismic wavelength by mass-movement processes. The magnitude of the diffraction energy could therefore provide an extra source of information to constrain flow type, for example to differentiate between debris flows (complete disaggregation and destruction of pre-failure internal interfaces), slumps (pre-failure internal interfaces deformed but largely preserved) and the transition between both end members. The high amplitude diffraction image response observed in Fig. 6b supports an interpretation of MTC A as a “structured” rather than “structureless” deposit, even if the geometry of such structure is not well-resolved by the seismic profiles used in this study.

We also resolve two normal fault planes *below* MTC A in the diffraction image (labelled “d” in Fig. 6). One is associated with a $\sim$500 m wide, channel-shaped depression on the top surface of MTC A around CMP 3750. We interpret these faults to be the result of sediment loading due to the emplacement of MTC A on the previously competent sediments, as the faults become blind at depth. As well as resolving structure within MTCs, diffraction imaging is able to image small-scale, discontinuous structure in the unfailed sediments immediately *below* the basal shear surface.

5.2 Discrimination of Events Near the Limit of Seismic Resolution

The Infante Don Henrique basin hosts a >1 s TWTT thick succession of stacked MTCs (Fig. 8). Some large events in profile MP06b ($n = 6$) are clearly visible on the full-wavefield seismic image as apparently chaotic bodies with well-defined top and basal reflectors. The diffraction image, however, reveals several smaller events ($n = 3$) that are difficult to identify or are ambiguous in the full-wavefield seismic image and associated discontinuity attributes. We interpret these events as MTCs, because they are associated with high amplitude reflectors (characteristic of the top and basal surfaces) and their diffraction response has relatively sharp boundaries, which would indicate they are not, for example, more extensive regional erosive unconformities. Nonetheless, it is important to remember that diffraction images only identify small-scale heterogeneous geology—they are not directly diagnostic for MTCs. Features with a similar diffraction response could include slightly erosional (e.g., furrowed) surfaces, such as those associated with turbidity currents.

In addition, the diffraction image allows for better definition of the apparent lateral extent (runout) of bodies. We are able to follow the apparent in-profile runout of some events for significant extra distance (on the order of kilometres for seismic profile MP06b) compared to the full-wavefield seismic image (Fig. 8f). We also observe this effect on seismic profile INS2-Line1 (Fig. 6) where there is a small MTC (MTC D, labelled "f" in Fig. 6) below the larger event, MTC A. In the full-wavefield seismic image, MTC D is represented by a short (less than 500 m), high amplitude basal horizon. The diffraction image shows a lobe shaped zone of heterogeneity, ∼3 km in length, that we interpret as a small MTC that failed towards the north, originating from the dome associated with the Lolita salt diapir.

Diffraction images in general offer higher lateral (i.e., horizontal) resolution because they overcome the lateral resolution limit of seismic reflections. In the context of screening for MTCs, diffraction images also improve the discrimination of relatively small, thin events (on the order of 10 ms TWTT thick, Fig. 8). This improvement is a result of removing the relatively high amplitude reflections, which can mask thin zones of discontinuous geology. In the MP06b profile, the unfailed confining sediments have a seismic character dominated by high amplitude, long wavelength reflections that are parallel to the MTCs. In addition, the MTCs themselves generate strong reflections at their top and basal surfaces. The apparent vertical thickness of these reflections is related to the dominant wavelength of the seismic source and is independent of the true thickness of the body. This means that the relatively high amplitude and long wavelength reflections can obscure thin, discontinuous geobodies that may otherwise be properly imaged by full-wavefield seismic imaging. By eliminating these masking reflections, the effective *interpretable* vertical resolution is increased for discontinuous, diffraction generating bodies that are thinner than the dominant seismic wavelength.

Consequently, diffraction images allow more accurate delineation of the total lateral extent of MTCs when a significant proportion of the body is thinner than the reflection image can resolve. This is particularly important to characterise the flow properties of unconfined mass-movements from seismic data. Many events have a substantial component of fine sediment that runs out a significant distance beyond the main cohesive body of the event, pinching out at zero thickness at the true maximum extent of the flow. This type of thin deposit, parallel to the background sedimentation, is difficult to image with full-wavefield seismic images for the reasons outlined above.

The record of buried MTCs identified from marine geophysical data is biased toward events that can be clearly resolved in multi-channel seismic reflection images (i.e., relatively thick and laterally extensive). This means that catalogues of MTCs are biased towards larger events, or younger events that are still preserved in the bathymetry (Urgeles & Camerlenghi, 2013). Screening for MTCs using diffraction imaging will allow for a more complete catalogue of smaller, deeper events, with more confident estimation of their true total runout.

5.3 Comparison to Seismic Discontinuity Attributes

Seismic discontinuity attributes are routinely computed as part of a traditional geohazard interpretation workflow in order to screen for, characterise and delineate MTCs (e.g., Alves et al., 2014; Bhatnagar et al., 2019). Here, we calculate the similarity and chaos attributes of the full-wavefield seismic image to compare to the diffraction image (Fig. 8). There are high-level similarities: areas with low similarity and high chaos values tend to correspond to areas of high diffraction energy. Relatively large events (MTC3, MTC4 and MTC8) are clearly imaged by both attributes and by the diffraction image. Several smaller events, however, are not clearly delineated from the background geology by the discontinuity attributes. Moreover, both the chaos and similarity attribute seem to be sensitive to features other than geological discontinuities—we observe low similarity, high chaos values for high amplitude, laterally continuous horizons (i.e., reflections) in the unfailed sediments that host the MTCs. It is difficult to discriminate a high amplitude, horizontal unfailed horizon from a thin MTC using these discontinuity attributes.

Preine et al. (2020) suggest that diffraction images may be a more "physically correct" alternative to using traditional discontinuity attributes to support interpretation of faults and fractures. We argue that this is also the case for interpretation of MTCs, because diffraction images:

1. are directly sensitive to the target geology (i.e., bodies likely to contain wavelength and sub-wavelength scale discontinuities).

2. eliminate relatively high amplitude, long wavelength coherent reflections—which can interfere with attributes and mask thin bodies.
3. do not suffer from edge effects and smoothing that may be introduced by window-based attributes.

5.4 Constraining the Lateral Extent of MTCs From 2-D Profiles

Seismic imaging in 2-D assumes that the recorded energy is reflected or diffracted from the 2-D vertical plane along the seismic profile. This may be a reasonable assumption where geological structure is 1-D perpendicular to the plane of the profile (a so-called *dip line*). When reflectors dip obliquely with respect to the profile, reflections cannot be properly imaged with a 2-D migration. Energy reflected from out-of-plane is not properly located in TWTT and may interfere with primary in-plane energy. MTCs are inherently 3-D geobodies—in addition to internal structure, they often show rugose, non-conformal upper and basal surfaces and steep, erosive lateral margins that can generate high amplitude reflections and diffractions (Fig. 1). This means that there is rarely an optimal direction to acquire a well-imaged 2-D seismic "dip line" across an MTC. In other words, out-of-plane energy is a common feature of 2-D seismic images of MTCs. The superior illumination of diffractions means that diffraction images will contain proportionally more out-of-plane energy than full-wavefield images.

Fig. 9 demonstrates this effect with a controlled synthetic test, where an MTC body is simulated as a half-ellipsoidal zone of point diffractors. The results show that while a 3-D migration is properly able to image and locate diffractors in space, a 2-D seismic acquisition and image will inevitably contain a large proportion of out-of-plane diffractions. The 2-D migrated section (Fig. 9d) shows an apparently "chaotic" texture, despite there being no chaotic reflectors inside the MTC. We speculate that out-of-plane diffractions could be partly responsible for the commonly observed apparently chaotic internal seismic response of MTCs in 2-D seismic profiles. This result underlines the importance of acquiring 3-D seismic data for good imaging and proper reconstruction of the geometry of the internal structure of MTCs, both for conventional full-wavefield seismic imaging and for diffraction imaging.

In Section 3.4 we propose a simple workflow to constrain the original location of out-of-plane diffracted energy imaged in a 2-D seismic profile. Under certain (strong) assumptions the results can be used to estimate a minimum bound on the lateral extent, perpendicular to the profile, of the zone of diffractors that contribute to the diffraction image—a constraint on the minimum half-width of an MTC imaged by a 2-D seismic profile. The controlled synthetic test shows that Eq. 1 can predict the apparent thickness of this diffraction shadow (Fig. 9d). We also demonstrate the method on a real data example by applying it to profile INS2-Line1, where there is a visible diffraction shadow beneath MTC A (Fig. 10). The presence of diffractions associated with MTC A, but beneath its apparent basal surface, indicates that the diffraction image contains energy from outside the plane of the profile. Does this real data example satisfy the assumptions stated in Section 3.4? It seems reasonable to assume that this MTC does contain diffractors spread throughout the body, as we consistently see an elevated response in the diffraction image throughout the 2-D profile in a downslope direction (Fig. 6). The maximum TWTT thickness of MTC A is $\sim$150 ms at a depth of $\sim$1.7 s TWTT, therefore we can consider this MTC to be a "thin body". MTC A is exposed at the seafloor, so we can be confident that the overburden velocity is constant (water velocity) and laterally homogeneous perpendicular to the profile. The remaining assumption is that there exists a well defined diffraction shadow associated with the body. In the lower part of the body, the diffraction shadow appears to be associated with MTC A, like in the controlled synthetic test. In the upper part of the body, however, there is significant uncertainty around whether the intepreted diffractors are associated with the MTC. For this real data example, the resulting zone of potential diffractors has half-width comparable to or lower than the distance to the edge of MTC A in the direction of maximum extent (Fig. 10d). This indicates that perhaps this zone of potential diffractors could be a realistic lower bound on the width of the MTC with respect to the seismic profile. On the other hand, interpreting the base of the diffraction shadow will always be the part of this workflow that introduces the greatest uncertainty. Even though this is a crude technique, with large errors, it is still an informative exercise to think about where these out-of-plane diffractors could come from, and how this relates to the overall geometry of an imaged MTC.

The method proposed in Section 3.4 is simple but nevertheless could be a useful way to estimate a lower bound on the extent of an MTC from a single 2-D seismic profile, where other geophysical information is not available. This is a common scenario when screening for MTCs for marine geohazard studies in frontier areas; for academic and vintage datasets; and in polar areas, where acquiring 3-D towed-streamer seismic data may be impossible due to year-round ice cover. It is trivial to extend the method to deal with buried MTCs, so long as i) the velocity model to the top of the body is known; ii) the slide is thin relative to its depth; and iii) the topography of the top surface is small, relative to its depth. Future studies should validate this approach for a realistic scenario by repeating the workflow for the controlled synthetic test with a 2-D profile extracted from a real data 3-D volume.

5.5 Limitations of Diffraction Imaging to Characterise MTCs

Whilst we have shown that diffraction images offer better imaging of small-scale discontinuous geology compared to reflection images, there remain some limitations, particularly regarding the data used for this study and the specific application to characterise MTCs.

5.5.1 Incomplete Diffraction Separation

Diffraction imaging relies on good separation between the diffracted and reflected wavefields. Here, we perform the diffraction separation in common-offset domain using PWD filters to eliminate laterally continuous reflections. Subaqueous mass-failures tend to occur in environments that are geologically complex, such as canyons, tectonically active areas and diapiric areas. In such environments, seismic images are likely to contain strong variation in dip, reflections that are not laterally continuous and high amplitude reflections and diffraction tails generated by a rugose seafloor. These factors can prevent reliable estimation of the true dip field from unmigrated seismic profiles. Our solution is to estimate the dip field on migrated data, and de-migrate the dip field for diffraction separation on the unmigrated common-offset sections. In general, the results of the dip estimation and de-migration are adequate for diffraction separation to image the shallow MTCs in this study. There are, however, some residual reflections that are not eliminated during diffraction separation, contaminating the diffraction images (Section 4.1). In practice, these can often be identified by carefully comparing the full-wavefield and diffraction images, as residual reflections will migrate to the same location and TWTT in both.

Other diffraction separation methods may be better suited to imaging MTCs in geologically complex settings. These include post-migration diffraction separation in dip-angle domain (Reshef & Landa, 2009) and diffraction separation by adaptive subtraction of the coherent reflected wavefield (Schwarz, 2019a). The choice of method ultimately depends on the seismic acquisition (e.g., streamer length compared to target depth, lateral and vertical image resolution, 2-D vs 3-D acquisition geometry), data characteristics (e.g., amplitude of diffractions relative to reflections, signal-to-noise level) and confidence in the velocity model. In all cases, the pre-processing flow must be designed to preserve diffraction energy.

5.5.2 Migration Velocities

For the seismic profiles analysed in this study, migration velocity analysis by focusing diffractions or moveout analysis of reflections was not possible (Section 3.3). The data were acquired using a short streamer relative to the water depth, so there is no significant differential moveout of reflection events in common-midpoint domain to perform a robust semblance-based velocity analysis. We found that the separated diffracted wavefield was routinely contaminated with out-of-plane diffractions, which would focus diffractions at an incorrect velocity and at an incorrect TWTT. Instead, we used migration velocities derived from simple velocity gradients in the shallow sediments, as our target MTCs are shallow with respect to the water depth. A test of the sensitivity of diffraction imaging to the chosen migration velocity is presented in the supplementary information (Fig. S7).

Future studies should concentrate on mitigating the effect of out-of-plane diffractions for focusing migration velocity analysis from 2-D seismic profiles (e.g., Preine et al., 2020). This could be achieved by weighting the focusing analysis towards continuous diffraction generating structures such as faults, or deeper diffractors that are less biased by not being exactly in-plane The problem of out-of-plane diffractions is resolved with 3-D seismic data, because 3-D migrations can collapse diffractions to their true apex.

6 Conclusions

In this study we use two 2-D marine multi-channel seismic profiles from the Gulf of Cadiz (south west Iberian Margin) to compare the ability of seismic diffraction imaging to conventional full-wavefield seismic imaging to characterise MTCs. Diffraction images can be considered to primarily image small-scale, discontinuous geological structure and have higher lateral resolution in comparison to full-wavefield seismic images. We find that in these examples MTCs generate a large contribution of diffracted energy compared to the surrounding unfailed confining sediments, likely because the scale of their internal structure and rugose erosional basal surface is close to, or below, the scale of the seismic wavelength.

Our results suggest that diffraction imaging can:

1. image internal structure of MTCs that is not well resolved by full-wavefield seismic images.
2. be used to better estimate the full extent of MTCs which have thin runout and to identify small events that are close to the resolution of the full-wavefield seismic image.
3. be a constraint on the overall scale of internal heterogeneity, important to classify flow type for MTCs that show an apparently chaotic or transparent seismic response.
4. be considered as a more physically justified alternative to traditional seismic discontinuity attributes to support interpretation of MTCs.

In addition, we show that 2-D diffraction images of MTCs are likely to include significant contributions of misplaced out-of-plane diffracted energy due to the inherently 3-D nature of MTCs. We suggest that, under certain strong assumptions, this energy (usually considered noise) may be used to constrain the 3-D geometry of MTCs from single 2-D seismic profiles by providing a minimum bound on the cross-line width. We demonstrate this using a controlled synthetic test and on one of the real data profiles.

Characterisation of MTCs and their internal structure is a promising new application of diffraction imaging, potentially bridging the "resolution gap" between seismic data and outcrop studies. Our results underline the importance of preserving diffractions through the processing flow for lateral resolution (including for full-wavefield seismic images), and the importance of 3-D seismic imaging to properly characterise complex geology such as MTCs. Better imaging provides important constraints on the failure and emplacement dynamics of MTCs, crucial for improving our understanding of the geohazard posed by subaqueous mass-movements.

Appendix A Dip De-migration

The aim of dip de-migration is to recover the unmigrated dip field from a dip field estimated on a migrated image. We use this technique due to the presence of high amplitude, steeply dipping diffraction tails and poor reflector continuity throughout the unmigrated data used in this study.

We perform the dip de-migration using simple geometric relations that describe how migration affects dipping reflectors in 2-D (Yilmaz, 2001):

1. The dip in a migrated section is greater than in the unmigrated section (migration *steepens* reflectors).
2. For areas of non-zero local dip the horizontal distance between points is shorter after migration.
3. Migration moves events in an up-dip direction.

After Chun and Jacewitz (1981), for migrated dip α', unmigrated dip α, local migration velocity, v, and TWTT t:

$$\begin{aligned}
\alpha' &= \frac{\alpha}{\sqrt{1-(\frac{\alpha v(x,t)}{2})^2}} \\
x' &= \frac{v(x,t)^2 t}{4}\alpha \\
t' &= t\left(1-\sqrt{1-\frac{\alpha v(x,t)}{2}}\right).
\end{aligned} \tag{A1}$$

We first solve for the un-migrated local dip value, $\alpha(x', t')$. Then we calculate the horizontal and vertical (time) shift ($x'-x$ and $t'-t$). The de-migrated dip field $\alpha(x, t)$ is estimated by applying image warping (with the horizontal and vertical shifts) to $\alpha(x', t')$. The effect is to reverse the effect of migration on the dip field, to "de-migrate" the dip field.

Acknowledgments

Pre-processed pre-stack seismic data, processing horizons, migration velocities and code to reproduce the results using Madagascar (Fomel et al., 2013) are archived in Ford (2020).

The authors wish to thank the crew, technicians and scientific party of the INSIGHT cruises (Legs 1 and 2), particularly the onboard seismic processing team: R. Bartolomé,

P. Brito, A. Calahorrano and E. Piazza. We are grateful to J. Preine, an anonymous reviewer and the associate editor for thoughtful and constructive reviews which significantly improved the quality of this article. Data for this study was collected in the framework of the project INSIGHT (CTM2015-70155-R) funded by the Spanish "Ministerio de Ciencia e Innovación" and the European Regional Development Fund. J. Ford was supported by a Marie Curie Doctoral Fellowship through the SLATE Innovative Training Network within the European Union Framework Programme for Research and Innovation Horizon 2020 under Grant Agreement No. 721403.

References

Alsop, G. I., & Marco, S. (2013). Seismogenic slump folds formed by gravity-driven tectonics down a negligible subaqueous slope. *Tectonophysics*, *605*(48-69), 48–69. doi: 10.1016/j.tecto.2013.04.004

Alves, T. M., Kurtev, K., Moore, G. F., & Strasser, M. (2014). Assessing the internal character, reservoir potential, and seal competence of mass-transport deposits using seismic texture: A geophysical and petrophysical approach. *AAPG Bulletin*, *98*(4), 793–824. doi: 10.1306/09121313117

Badhani, S., Cattaneo, A., Collico, S., Urgeles, R., Dennielou, B., Leroux, E., ... Droz, L. (2020). Integrated geophysical, sedimentological and geotechnical investigation of submarine landslides in the Gulf of Lions (Western Mediterranean). *Geological Society, London, Special Publications*, *500*(1), 359–376. doi: 10.1144/SP500-2019-175

Baptista, M., Heitor, S., Miranda, J., Miranda, P., & Victor, L. (1998). The 1755 Lisbon tsunami; evaluation of the tsunami parameters. *Journal of Geodynamics*, *25*(1-2), 143–157. doi: 10.1016/S0264-3707(97)00019-7

Baptista, M., & Miranda, J. (2009). Revision of the Portuguese catalog of tsunamis. *Natural Hazards and Earth System Sciences*, *9*(1), 25–42. doi: 10.5194/nhess-9-25-2009

Berndt, C., Costa, S., Canals, M., Camerlenghi, A., de Mol, B., & Saunders, M. (2012). Repeated slope failure linked to fluid migration: The Ana submarine landslide complex, Eivissa Channel, Western Mediterranean Sea. *Earth and Planetary Science Letters*, *319-320*, 65–74. doi: 10.1016/j.epsl.2011.11.045

Bhatnagar, P., Verma, S., & Bianco, R. (2019). Characterization of mass transport deposits using seismic attributes: Upper Leonard Formation, Permian Basin. *Interpretation*, *7*(4), SK19–SK32. doi: 10.1190/INT-2019-0036.1

Born, M., & Wolf, E. (1959). *Principles of optics: Electromagnetic theory of propagation, interference, and diffraction of light.* London: Pergamon Press.

Brackenridge, R. E., Hernández-Molina, F. J., Stow, D. A. V., & Llave, E. (2013). A Pliocene mixed contourite–turbidite system offshore the Algarve Margin, Gulf of Cadiz: Seismic response, margin evolution and reservoir implications. *Marine and Petroleum Geology*, *46*, 36–50. doi: 10.1016/j.marpetgeo.2013.05.015

Bull, S., Cartwright, J., & Huuse, M. (2009). A review of kinematic indicators from mass-transport complexes using 3D seismic data. *Marine and Petroleum Geology*, *26*(7), 1132–1151. doi: 10.1016/j.marpetgeo.2008.09.011

Bull, S., & Cartwright, J. A. (2020). Line length balancing to evaluate multi-phase submarine landslide development: an example from the Storegga Slide, Norway. *Geological Society, London, Special Publications*, *500*(1), 531–549. doi: 10.1144/SP500-2019-168

Cardona, S., Wood, L. J., Day-Stirrat, R. J., & Moscardelli, L. (2016). Fabric Development and Pore-Throat Reduction in a Mass-Transport Deposit in the Jubilee Gas Field, Eastern Gulf of Mexico: Consequences for the Sealing Capacity of MTDs. In G. Lamarche et al. (Eds.), *Submarine Mass Movements and their Consequences* (Vol. 41, pp. 27–37). Cham: Springer. doi: 10.1007/978-3-319-20979-1_3

Carter, L., Gavey, R., Talling, P., & Liu, J. (2014). Insights into Submarine Geohazards from Breaks in Subsea Telecommunication Cables. *Oceanography*, *27*(2), 58–67. doi: 10.5670/oceanog.2014.40

Chen, J., & Schuster, G. T. (1999). Resolution limits of migrated images. *GEOPHYSICS*, *64*(4), 1046–1053. doi: 10.1190/1.1444612

Chopra, S., & Marfurt, K. J. (2007). *Seismic Attributes for Prospect Identification and Reservoir Characterization.* Tulsa, OK: Society of Exploration Geophysicists. doi: 10.1190/1.9781560801900

Chun, J. H., & Jacewitz, C. A. (1981). Fundamentals of frequency domain migration. *GEOPHYSICS*, *46*(5), 717–733. doi: 10.1190/1.1441211

Claerbout, J. F. (1992). *Earth Soundings Analysis: Processing Versus Inversion.* London: Blackwell Scientific Publications.

Decker, L., Janson, X., & Fomel, S. (2015). Carbonate reservoir characterization using seismic diffraction imaging. *Interpretation*, *3*(1), SF21–SF30. doi: 10.1190/INT-2014-0081.1

Decker, L., Merzlikin, D., & Fomel, S. (2017). Diffraction imaging and time-migration velocity analysis using oriented velocity continuation. *GEOPHYSICS*, *82*(2), U25-U35. doi: 10.1190/geo2016-0141.1

Dell, S., & Gajewski, D. (2011). Common-reflection-surface-based workflow for diffraction imaging. *GEOPHYSICS*, *76*(5), S187–S195. doi: 10.1190/geo2010-0229.1

Diviacco, P., Rebesco, M., & Camerlenghi, A. (2006). Late Pliocene Mega Debris Flow Deposit and Related Fluid Escapes Identified on the Antarctic Peninsula Continental Margin by Seismic Reflection Data Analysis. *Marine Geophysical Researches*, *27*(2), 109–128. doi: 10.1007/s11001-005-3136-8

Fomel, S. (2002). Applications of plane-wave destruction filters. *GEOPHYSICS*, *67*(6), 1946–1960. doi: 10.1190/1.1527095

Fomel, S., Landa, E., & Taner, M. (2007). Poststack velocity analysis by separation and imaging of seismic diffractions. *GEOPHYSICS*, *72*(6), U89-U94. doi: 10.1190/1.2781533

Fomel, S., Sava, P., Vlad, I., Liu, Y., & Bashkardin, V. (2013). Madagascar: open-source software project for multidimensional data analysis and reproducible computational experiments. *Journal of Open Research Software*, *1*(1), e8. doi: 10.5334/jors.ag

Ford, J. (2020). *Multi-channel seismic reflection profiles MP06b and INS-Line1 (INSIGHT cruises).* Zenodo. (Dataset) doi: 10.5281/zenodo.3946170

Frey Martinez, J., Cartwright, J., & Hall, B. (2005). 3D seismic interpretation of slump complexes: examples from the continental margin of Israel. *Basin Research*, *17*(1), 83–108. doi: 10.1111/j.1365-2117.2005.00255.x

Gafeira, J., Long, D., Scrutton, R., & Evans, D. (2010). 3D seismic evidence of internal structure within Tampen Slide deposits on the North Sea Fan: are chaotic deposits that chaotic? *Journal of the Geological Society*, *167*(3), 605–616. doi: 10.1144/0016-76492009-047

Gazdag, J., & Sguazzero, P. (1984). Migration of seismic data by phase shift plus interpolation. *GEOPHYSICS*, *49*(2), 124–131. doi: 10.1190/1.1441643

Gràcia, E., Dañobeitia, J., Vergés, J., Bartolomé, R., & Córdoba, D. (2003). Crustal architecture and tectonic evolution of the Gulf of Cadiz (SW Iberian margin) at the convergence of the Eurasian and African plates. *Tectonics*, *22*(4). doi: 10.1029/2001TC901045

Gràcia, E., Dañobeitia, J., Vergés, J., & Team, P. (2003). Mapping active faults offshore Portugal (36N–38N): Implications for seismic hazard assessment along the southwest Iberian margin. *Geology*, *31*(1), 83. doi: 10.1130/0091-7613(2003)031⟨0083:MAFOPN⟩2.0.CO;2

Gràcia, E., Urgeles, R., Rothenbeck, M., Wenzlaff, E., Steinführer, A., Kurbjuhn, T., … INSIGHT Leg 1 cruise party (2018). *ImagiNg large SeismogenIc and tsunamiGenic structures of the Gulf of Cadiz with ultra-High resolution Technologies (INSIGHT) Leg 1 survey cruise report* (Tech. Rep.). Institut de Ciències del Mar - CSIC.

Gràcia, E., Vizcaino, A., Escutia, C., Asioli, A., Rodés, Á., Pallàs, R., … Goldfinger, C. (2010). Holocene earthquake record offshore Portugal (SW Iberia): testing turbidite paleoseismology in a slow-convergence margin. *Quaternary Science Reviews*, *29*(9-10), 1156–1172. doi: 10.1016/j.quascirev.2010.01.010

Harlan, W. S., Claerbout, J. F., & Rocca, F. (1984). Signal/noise separation and velocity estimation. *GEOPHYSICS*, *49*(11), 1869–1880. doi: 10.1190/1.1441600

Karstens, J., Berndt, C., Urlaub, M., Watt, S. F., Micallef, A., Ray, M., … Brune, S. (2019). From gradual spreading to catastrophic collapse – Reconstruction of the 1888 Ritter Island volcanic sector collapse from high-resolution 3D seismic data. *Earth and Planetary Science Letters*, *517*, 1–13. doi: 10.1016/j.epsl.2019.04.009

Kessinger, W. (1992). Extended split-step Fourier migration. In *SEG Technical Program Expanded Abstracts 1992* (pp. 917–920). Tulsa, OK: Society of Exploration Geophysicists. doi: 10.1190/1.1822254

Khaidukov, V., Landa, E., & Moser, T. (2004). Diffraction imaging by focusing-defocusing: An outlook on seismic superresolution. *GEOPHYSICS*, *69*(6), 1478–1490. doi: 10.1190/1.1836821

Klem-Musatov, K., Hoeber, H., Pelissier, M., & Moser, T. J. (Eds.). (2016). *Seismic Diffraction*. Tulsa, OK: Society of Exploration Geophysicists. doi: 10.1190/1.9781560803188

Lackey, J., Moore, G., & Strasser, M. (2018). Three-dimensional mapping and kinematic characterization of mass transport deposits along the outer Kumano Basin and Nankai accretionary wedge, southwest Japan. *Progress in Earth and Planetary Science*, *5*(1), 65. doi: 10.1186/s40645-018-0223-4

Leynaud, D., Mulder, T., Hanquiez, V., Gonthier, E., & Régert, A. (2017). Sediment failure types, preconditions and triggering factors in the Gulf of Cadiz. *Landslides*, *14*(1), 233–248. doi: 10.1007/s10346-015-0674-2

Lo Iacono, C., Gràcia, E., Zaniboni, F., Pagnoni, G., Tinti, S., Bartolome, R., ... Zitellini, N. (2012). Large, deepwater slope failures: Implications for landslide-generated tsunamis. *Geology*, *40*(10), 931–934. doi: 10.1130/G33446.1

Lucente, C. C., & Pini, G. A. (2003). Anatomy and emplacement mechanism of a large submarine slide within a Miocene foredeep in the northern Apennines, Italy: A field perspective. *American Journal of Science*, *303*(7), 565–602. doi: 10.2475/ajs.303.7.565

Lumley, D. E., Claerbout, J. F., & Bevc, D. (1994). Anti-aliased Kirchhoff 3-D migration. In *SEG Technical Program Expanded Abstracts 1994* (pp. 1282–1285). Society of Exploration Geophysicists. doi: 10.1190/1.1822760

Matias, L. M., Cunha, T., Annunziato, A., Baptista, M. A., & Carrilho, F. (2013). Tsunamigenic earthquakes in the Gulf of Cadiz: fault model and recurrence. *Natural Hazards and Earth System Sciences*, *13*(1), 1–13. doi: 10.5194/nhess-13-1-2013

Medialdea, T., Somoza, L., Pinheiro, L., Fernández-Puga, M., Vázquez, J., León, R., ... Vegas, R. (2009). Tectonics and mud volcano development in the Gulf of Cádiz. *Marine Geology*, *261*(1-4), 48–63. doi: 10.1016/j.margeo.2008.10.007

Moser, T., & Howard, C. (2008). Diffraction imaging in depth. *Geophysical Prospecting*, *56*(5), 627–641. doi: 10.1111/j.1365-2478.2007.00718.x

Mulder, T., & Cochonat, P. (1996). Classification of offshore mass movements. *Journal of Sedimentary Research*, *66*(1), 43–57. doi: 10.1306/D42682AC-2B26-11D7-8648000102C1865D

Mulder, T., Gonthier, E., Lecroart, P., Hanquiez, V., Marches, E., & Voisset, M. (2009). Sediment failures and flows in the Gulf of Cadiz (eastern Atlantic). *Marine and Petroleum Geology*, *26*(5), 660–672. doi: 10.1016/j.marpetgeo.2008.02.009

Piper, D. J. W., Cochonat, P., & Morrison, M. L. (1999). The sequence of events around the epicentre of the 1929 Grand Banks earthquake: initiation of debris flows and turbidity current inferred from sidescan sonar. *Sedimentology*, *46*(1), 79–97. doi: 10.1046/j.1365-3091.1999.00204.x

Piper, D. J. W., Pirmez, C., Manley, P. L., Long, D., Flood, R. D., Normark, W. R., & Showers, W. (1997). Mass-transport deposits of the Amazon fan. *Proceedings of the Ocean Drilling Program. Scientific results*, *155*, 109–146.

Posamentier, H. W., & Martinsen, O. J. (2011). The Character and Genesis of Submarine Mass-Transport Deposits: Insights from Outcrop and 3D Seismic Data. In R. C. Shipp, P. Weimer, & H. W. Posamentier (Eds.), *Mass-Transport Deposits in Deepwater Settings.* SEPM (Society for Sedimentary Geology). doi: 10.2110/sepmsp.096.007

Preine, J., Schwarz, B., Bauer, A., & Hübscher, C. (2020). When There Is No Offset: A Demonstration of Seismic Diffraction Imaging and Depth-Velocity Model Building in the Southern Aegean Sea. *Journal of Geophysical Research: Solid Earth*, *125*(9), e2020JB019961. doi: 10.1029/2020JB019961

Prior, D. B., Bornhold, B. D., & Johns, M. W. (1984). Depositional Characteristics of a Submarine Debris Flow. *The Journal of Geology*, *92*(6), 707–727. doi: 10.1086/628907

Reshef, M., & Landa, E. (2009). Post-stack velocity analysis in the dip-angle domain using diffractions. *Geophysical Prospecting*, *57*(5), 811–821. doi: 10.1111/j.1365-2478.2008.00773.x

Satake, K. (2012). Tsunamis Generated by Submarine Landslides. In Y. Yamada et al. (Eds.), *Submarine Mass Movements and Their Consequences* (pp. 475–484). Dordrecht: Springer Netherlands. doi: 10.1007/978-94-007-2162-3_42

Sawyer, D. E., Flemings, P. B., Dugan, B., & Germaine, J. T. (2009). Retrogressive failures recorded in mass transport deposits in the Ursa Basin, Northern Gulf of Mexico. *Journal of Geophysical Research: Solid Earth*, *114*(B10). doi: 10.1029/2008JB006159

Schwarz, B. (2019a). Coherent wavefield subtraction for diffraction separation. *GEOPHYSICS*, *84*(3), V157–V168. doi: 10.1190/geo2018-0368.1

Schwarz, B. (2019b). An introduction to seismic diffraction. In C. Schmelzbach (Ed.), *Recent advances in seismology* (Vol. 60, pp. 1–64). Elsevier. doi: 10

.1016/bs.agph.2019.05.001

Schwarz, B., & Gajewski, D. (2017). Accessing the diffracted wavefield by coherent subtraction. *Geophysical Journal International*, *211*(1), 45–49. doi: 10.1093/gji/ggx291

Schwarz, B., & Krawczyk, C. M. (2020). Coherent diffraction imaging for enhanced fault and fracture network characterization. *Solid Earth*, *11*(5), 1891–1907. doi: 10.5194/se-11-1891-2020

Shipp, R. C., Nott, J. A., & Newlin, J. A. (2004). Physical Characteristics and Impact of Mass Transport Complexes on Deepwater Jetted Conductors and Suction Anchor Piles. In *Offshore Technology Conference.* Houston, Texas: Offshore Technology Conference. doi: 10.4043/16751-MS

Silva, P., Roque, C., Drago, T., Belén, A., Henry, B., Gemma, E., ... Vázquez, J. (2020). Multidisciplinary characterization of Quaternary mass movement deposits in the Portimão Bank (Gulf of Cadiz, SW Iberia). *Marine Geology*, *420*, 106086. doi: 10.1016/j.margeo.2019.106086

Sobiesiak, M. S., Kneller, B., Alsop, G. I., & Milana, J. P. (2016). Internal deformation and kinematic indicators within a tripartite mass transport deposit, NW Argentina. *Sedimentary Geology*, *344*, 364–381. doi: 10.1016/j.sedgeo.2016.04.006

Steventon, M. J., Jackson, C. A.-L., Hodgson, D. M., & Johnson, H. D. (2019). Strain analysis of a seismically imaged mass-transport complex, offshore Uruguay. *Basin Research*, *31*(3), 600–620. doi: 10.1111/bre.12337

Stolt, R. H. (1978). Migration by Fourier transform. *GEOPHYSICS*, *43*(1), 23–48. doi: 10.1190/1.1440826

Talling, P. J., Wynn, R. B., Schmmidt, D. N., Rixon, R., Sumner, E., & Amy, L. (2010). How Did Thin Submarine Debris Flows Carry Boulder-Sized Intraclasts for Remarkable Distances Across Low Gradients to the Far Reaches of the Mississippi Fan? *Journal of Sedimentary Research*, *80*(10), 829–851. doi: 10.2110/jsr.2010.076

Taner, M., Fomel, S., & Landa, E. (2006). Separation and imaging of seismic diffractions using plane-wave decomposition. In *SEG Technical Program Expanded Abstracts 2006* (pp. 2401–2405). Tulsa, OK: Society of Exploration Geophysicists. doi: 10.1190/1.2370017

Tappin, D. R., Watts, P., McMurtry, G. M., Lafoy, Y., & Matsumoto, T. (2001). The Sissano, Papua New Guinea tsunami of July 1998 — offshore evidence on the source mechanism. *Marine Geology*, *175*(1), 1–23. doi: 10.1016/S0025-3227(01)00131-1

Terrinha, P., Pinheiro, L., Henriet, J.-P., Matias, L., Ivanov, M., Monteiro, J., ... Rovere, M. (2003). Tsunamigenic-seismogenic structures, neotectonics, sedimentary processes and slope instability on the southwest Portuguese Margin. *Marine Geology*, *195*(1-4), 55–73. doi: 10.1016/S0025-3227(02)00682-5

Urgeles, R., & Camerlenghi, A. (2013). Submarine landslides of the Mediterranean Sea: Trigger mechanisms, dynamics, and frequency-magnitude distribution. *Journal of Geophysical Research: Earth Surface*, *118*(4), 2013JF002720. doi: 10.1002/2013JF002720

Urgeles, R., INSIGHT Leg 2 cruise shipboard participants, et al. (2019). *ImagiNg large SeismogenIc and tsunamiGenic structures of the Gulf of Cadiz with ultra-High resolution Technologies (INSIGHT) Leg 2 survey cruise report* (Tech. Rep.). Institute of Marine Sciences, Barcelona.

Urgeles, R., Masson, D. G., Canals, M., Watts, A. B., & Bas, T. L. (1999). Recurrent large-scale landsliding on the west flank of La Palma, Canary Islands. *Journal of Geophysical Research: Solid Earth*, *104*(B11), 25331–25348. doi: 10.1029/1999JB900243

Vizcaino, A., Gràcia, E., Pallàs, R., Garcia-Orellana, J., Casas, D., Willmott, V., ... Asioli, A. (2006). Sedimentology, physical properties and age of mass transport deposits associated with the Marquês de Pombal Fault, Southwest Portuguese Margin. *Norwegian Journal of Geology*, *86*(3), 177-186.

Weimer, P., & Shipp, C. (2004). Mass Transport Complex: Musing on Past Uses and Suggestions for Future Directions. In *Offshore Technology Conference.* Houston, Texas: Offshore Technology Conference. doi: 10.4043/16752-MS

Yilmaz, O. (2001). *Seismic Data Analysis: Processing, Inversion, and Interpretation of Seismic Data.* Tulsa, OK: Society of Exploration Geophysicists. doi: 10.1190/1.9781560801580

Zitellini, N., Gràcia, E., Matias, L., Terrinha, P., Abreu, M., DeAlteriis, G., ... Mulder, T. (2009). The quest for the Africa–Eurasia plate boundary west of the Strait of Gibraltar. *Earth and Planetary Science Letters*, *280*(1-4), 13–50. doi:

10.1016/j.epsl.2008.12.005

Zitellini, N., Rovere, M., Terrinha, P., Chierici, F., & Matias, L. (2004). Neogene Through Quaternary Tectonic Reactivation of SW Iberian Passive Margin. *Pure and Applied Geophysics*, *161*(3), 565–587. doi: 10.1007/s00024-003-2463-4